# Supplementary Information

# Bistable Origami Thermal Switch with High Switching Ratios

Bowen Tan[1,2†], Jun Lyu[1†], Fuwei Yang[3], Ke Xu[1], Shuo Qiao[1], Bai Song[4,5], Lin Yang[1,5*], Ke Liu[1*]

[1]School of Advanced Manufacturing and Robotics, Peking University, Beijing 100871, China.

[2]School of Future Technology, Shandong University, Jinn 250002, China.

[3]Department of Engineering Mechanics, Tsinghua University, Beijing 100084, China.

[4]School of Mechanics and Engineering Science, Peking University, Beijing 100871, China.

[5]National Key Laboratory of Advanced Micro and Nano Manufacture Technology, Peking University, Beijing 100871, China.

## Supplementary Note 1: Geometry of the origami pattern

The BOS origami pattern can be constructed in six steps (Fig. S1). Below we show the process to make the pentagon-based design with 5 arms, as used in this work.

In the beginning, we estimate the general dimension of the device, and draw two circles with radii $a$ and $c$. Then we draw three regular pentagons based on the circles. The innermost pentagon is inscribed in the circle of radius $a$, and the outermost pentagon is inscribed in the circle of radius $c$. The middle regular pentagon is circumscribed about the inner circle, and we define the circumradius of this middle pentagon as $b$. The radius of $b$ is constrained to be:

$$b = a/cos\frac{\pi}{5} \tag{S1}$$

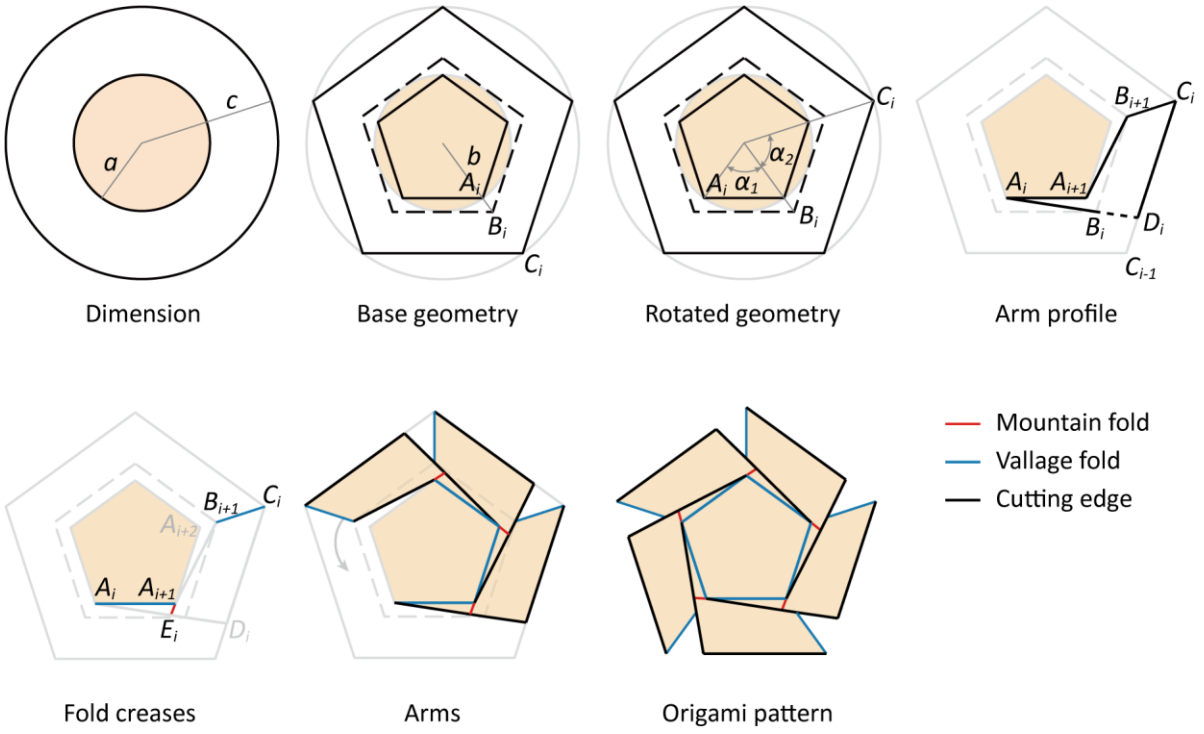


**Fig. S1.** Design of the BOS origami pattern

The design rationale is that $b$ must reduce the required width of the arm while also remaining larger than $a$. This condition enables an optimal arm design.

Here, let $A_i$, $B_i$, and $C_i$ denote the vertices of each pentagon for $i = \{0,1,2,3,4\}$. The top vertex of each pentagon is assigned to subscript 0, and other vertices are sorted counterclockwise.

$$\begin{cases} A_i = (a\cos\theta_i, a\sin\theta_i) \\ B_i = (b\cos\theta_i, b\sin\theta_i), \\ C_i = (c\cos\theta_i, c\sin\theta_i) \end{cases} \quad \text{(S2)}$$
$$\theta_i = \frac{\pi}{2} + \frac{2\pi i}{5}, i = 0,1,2,3,4$$

To form the arm, we use the vertices $\{A_i, B_i, C_i\}$ to determine the its profile and the three pentagons are rotated relative to one another. Two deviation angles $\alpha_1$ and $\alpha_2$ are defined between adjacent pentagons. Using the middle pentagon as a reference frame, the vertex coordinates are given by:

$$\begin{aligned} A_i &= \big(a\cos(\theta_i - \alpha_1), a\sin(\theta_i - \alpha_1)\big) \\ B_i &= (b\cos\theta_i, b\sin\theta_i) \\ C_i &= \big(c\cos(\theta_i + \alpha_2), c\sin(\theta_i + \alpha_2)\big) \end{aligned} \tag{S3}$$

The arm profile is derived from three positioning pentagons using vertices $\{A_i, A_{i+1}, B_{i+1}, C_i, B_i\}$. To increase load-bearing capacity, segment $A_iB_i$ is extended to a new point $D_i$, widening the arm. This results in a closed polygonal profile defined by vertices $\{A_i, A_{i+1}, B_{i+1}, C_i, D_i\}$, traversed cyclically.

$$D_i = B_i + \frac{\overrightarrow{A_iB_i}}{\|A_iB_i\|} l_{BD}, \qquad 0 < l_{BD} \le c - b \tag{S4}$$

$$\frac{A_iB_i}{\|A_iB_i\|} = \left(\frac{b\cos\theta_i - a\cos(\theta_i - \alpha_1)}{\sqrt{a^2 + b^2 - 2ab\cos\alpha_1}}, \frac{b\sin\theta_i - a\sin(\theta_i - \alpha_1)}{\sqrt{a^2 + b^2 - 2ab\cos\alpha_1}}\right) \tag{S5}$$

where $l_{BD}$ is the extension length from point $B_i$ to $D_i$, and we use $l_{BD}$ =0.78$(c - b)$.

To achieve the foldability of the origami pattern, three creases are designed on the

arm. Two of them are edges $A_iA_{i+1}$ and $C_iB_{i+1}$ which connect the arm to the pentagonal plate and to the ground. However, the arm's motion is currently constrained by panel deformation, which prevents relative movement at these two creases. To release this constraint, a third crease $A_{i+1}E_i$ is added perpendicular to the existing creases. Point $E_i$ lies on the interaction point of line $A_iD_i$, and the extension of edge $A_{i+1}A_{i+2}$ of the inner pentagon. This configuration leads to slight bending of the arm but reduces stress at the crease $A_{i+1}E_i$ to prevent damage. The intersection point $E_i$ is obtained by solving the system of equations shown below:

$$\begin{cases} E_i = A_{i+1} + \mu\overrightarrow{A_{i+1}A_{i+2}} \\ E_i = A_i + \eta\overrightarrow{A_iB_i} \end{cases} \tag{S6}$$

The solution of $\eta$ is given by:

$$\eta = \frac{(A_{i+1} - A_i) \times (A_{i+2} - A_{i+1})}{(B_i - A_i) \times (A_{i+2} - A_{i+1})} = \frac{2a\sin(\pi/5)\sin(2\pi/5)}{b\cos(3\pi/5 - \alpha_1) - a\cos(3\pi/5)} \tag{S7}$$

Substituting Eq. S7 into Eq. S6, the coordinate of point $E_i$ is

$$\begin{cases} E_{ix} = a\cos(\theta_i - \alpha_1) + \dfrac{4a \cdot \sin^2(\frac{\pi}{5}) \cdot \cos(\frac{\pi}{5}) \cdot (b\cos\theta_i - a\cos(\theta_i - \alpha_1))}{a\cos(\frac{2\pi}{5}) + b\cos(\frac{3\pi}{5} - \alpha_1)} \\ E_{iy} = a\sin(\theta_i - \alpha_1) + \dfrac{4a \cdot \sin^2(\frac{\pi}{5}) \cdot \cos(\frac{\pi}{5}) \cdot (b\sin\theta_i - a\sin(\theta_i - \alpha_1))}{a\cos(\frac{2\pi}{5}) + b\cos(\frac{3\pi}{5} - \alpha_1)} \end{cases} \quad \text{(S8)}$$

Finally, we generate points $\{A_i, B_i, C_i, D_i, E_i\}$ sequentially and connect their corresponding edges and creases, establishing the origami pattern for the bistable origami switch. This pattern features four design parameters ($a$, $c$, $\alpha_1$, and $\alpha_2$) and three calculated parameters ($b$, $l_{BD}$, $\eta$). Parameters $a$ and $c$ are determined by the dimensions of the device and switch. $\alpha_1$ and $\alpha_2$ govern the arm's shape: $\alpha_1$ controls height while $\alpha_2$ controls width.

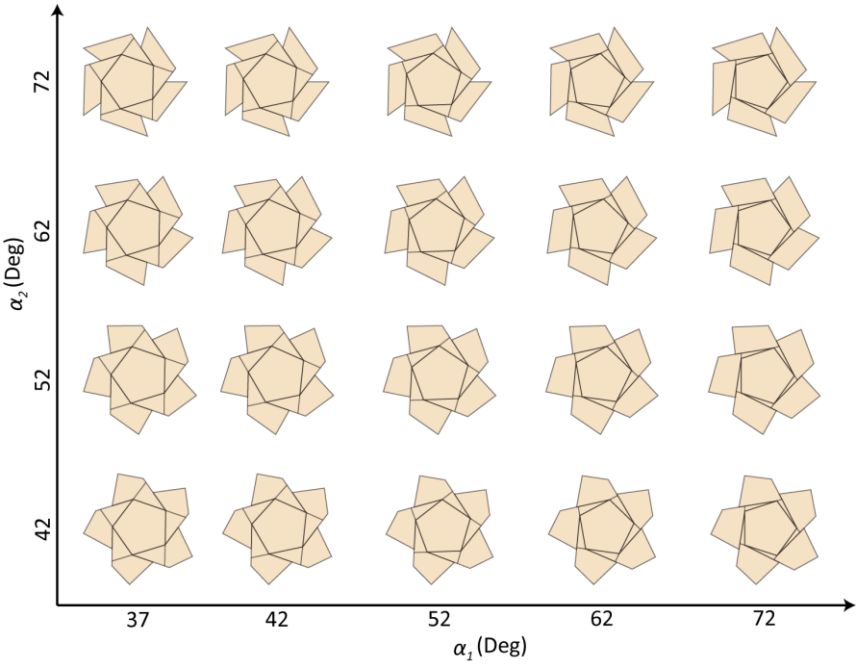


**Fig. S2.** Illustrations of design parameters $\alpha_1$ and $\alpha_2$ on the origami pattern.

**Supplementary Note 2: Fabrication of bistable origami metastructure**

A 0.2-mm-thick polyimide film (Guangzhou Shibei Dragon Electronics Co., Ltd., China) is selected as the base material. The film is laser-cut along the origami pattern (Fig. 1D) using a 16 W laser cutter. The design parameters of the origami pattern are set as $a$ = 20 mm, $b$ = 25 mm, $c$ = 40 mm, $\alpha_1$ = 59.2°, and $\alpha_2$ = 55°. Cut pieces are bonded using polyimide tape (3M™ 7418F Heat-Resistant Polyimide Process Tape). Fifteen 1-mm-diameter holes are drilled into the inner pentagon plate (three holes at each edge).

The thermal actuator (Fig. 3C) comprises a U-shape SMA wire (Beijing GEE SMA Technology Co., Ltd., China) and a stainless-steel torsional spring (Wenzhou Heli Spring Manufacturing Co., Ltd., China). The U-shape SMA wire has a length of 7.5 mm, width of 5 mm, and wire diameter of 0.5 mm. It is twisted 180° about its major axis and installed concentrically within the torsional spring. The torsional spring has a wire diameter of 0.4 mm, outer diameter of 3 mm, 9 coils, and an initial angle of 180°. The spring torque can be estimated by:

$$T = k\theta = \frac{Ed^4}{3667Dn}\theta \tag{S9}$$

where $E$ is the elastic module, $d$ is the wire diameter, $D$ is the mean diameter, $n$ denotes the number of coils, and $\theta$ represents angular deflection.

To mount the thermal actuator and facilitate heat transfer, a copper base is fabricated

using a 0.1-mm-thick copper plate (Xinghua Fangling Metal Products Co., Ltd., China) and copper sleeves (Taizhou Xuehua Stainless Steel Products Co., Ltd., China). The copper plate is cut to size matching the dimensions and arrangement of the inner pentagon pane. Copper sleeves (height: 3 mm, inner diameter: 1 mm, outer diameter: 2.2 mm) are welded over these holes. The sleeve bores are then filled with silicone grease (Shin-Etsu Chemical 7921), and a 0.8-mm-diameter TPU elastic cord (MIYUKI H3198E, length: 50 mm) is fastened to a corner sleeve. This integrated assembly of copper plate, sleeves, and TPU cord constitutes the regulator.

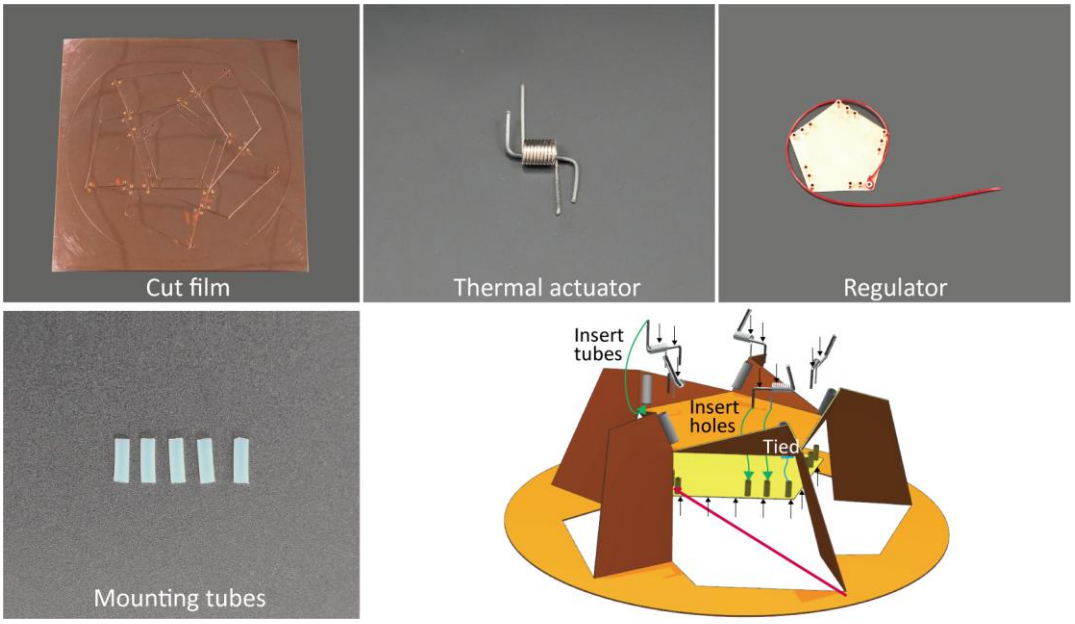


**Fig. S3.** Photographs of the BOS components and assembly.

Finally, the regulator's sleeves and TPU cord are secured to the polyimide film. The

thermal actuators are installed by inserting their wire ends into the copper sleeves, while the opposite ends engage mounting tubes. These mounting tubes are sections of Teflon tubing (inner diameter: 1.8 mm, outer diameter: 2.6 mm) cut to length of 5 mm. The Teflon tubes are permanently affixed to the origami arms via riveted connections.

**Supplementary Note 3: Mechanical characterization**

Mechanical tests are performed on a mechanical testing system (50-N load-cell, MARK-10).

**(1) Measurement of the bending modulus of polyimide film**

The bending modulus of the polyimide film is measured via customized three-point bending tests (Fig. S4). Sample dimensions are 80 mm (length) × 60 mm (width). The span $L$ of between fixed fulcrums is 51.9 mm. The bending modulus is calculated by(2):

$$E = \frac{L^3 F}{4bt^3 \delta} \tag{S10}$$

where $b$ is the width of the sample, $\delta$ is the midpoint deflection. Using the straight-line segment of the force-deflection curve, the bending modulus of the polyimide film is calculated as 4000 MPa.

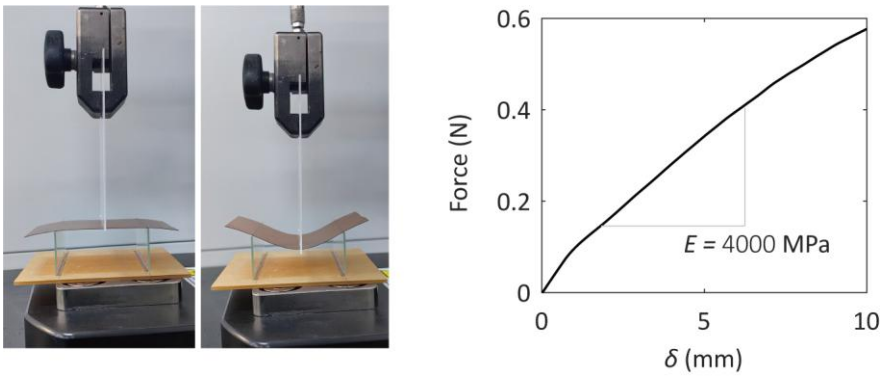


**Fig. S4.** Measurement of bending modulus of the polyimide film.

**(2) Measurement of the stiffness of the hinges**

To measure hinge stiffness, we fabricated a dedicated test sample using rigid plates and hinges identical to those in the BOS (Fig. S5). The sample consists of four acrylic plates (20 mm × 20 mm × 1 mm) joined with polyimide tape. Bonding surfaces are staggered sequentially between front and back sides, forming three identical hinges.

The sample is clamped between two fixtures of the testing machine. During testing, a crosshead displacement rate of 10 mm/min is applied while measuring force ($F$) and displacement ($\Delta d$). The bending moment $M_b$ at each hinge and corresponding folding angle change $\Delta\gamma$ were calculated by(1):

$$F\Delta d = M_b + 0.5M_b + 0.5M_b \tag{S11}$$

$$\Delta\gamma = 2\sin^{-1}\left(\frac{d_0}{2l}\right) - 2\sin^{-1}\left(\frac{d_0 - \Delta d}{2l}\right) \tag{S12}$$

where $d_0 = 40$ mm is the initial outer-hinge distance, and $l = 20$ mm is the acrylic plate length. The average rotational stiffness $k_\gamma = 0.0285$ N·mm/rad is derived by normalizing the slope of the bending moment-folding angle curve ($M_b$ vs. $\Delta\gamma$) to the tape width of 10 mm.

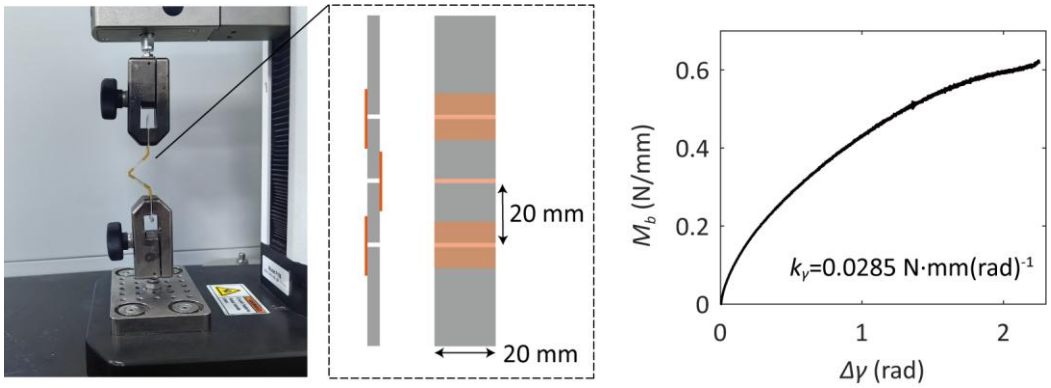


**Fig. S5.** Measurement of rotational stiffness of the hinges.

**(3) Measurement of the structural force of BOS**

To measure axial force while accommodating twist coupling in the BOS, we fabricated a low-friction rotational coupling between the BOS and testing machine clamp (Fig. S6). The coupling consists of a pentagonal copper plate mounted at the terminus of a slender bolt, constrained by locking nuts and washers. During testing, the BOS is initialized in its flat state, and then being vertically deployed at 10 mm/min via the clamp. Throughout deployment, axial displacement and force are recorded. The energy is subsequently calculated by integrating the force-displacement curve.

$$U = \int_0^{\delta} F \, d\delta \tag{S13}$$

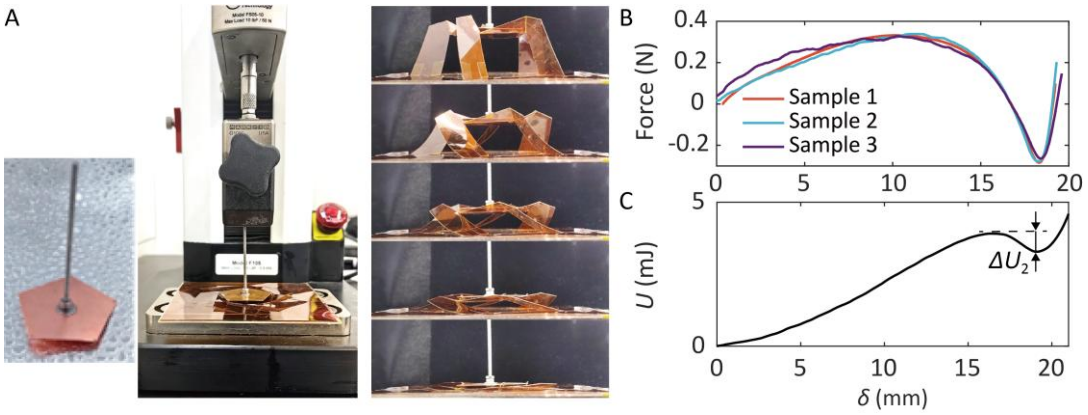


**Fig. S6.** Measurement of mechanical properties of BOS. (A) Photo of the experimental set-up. (B) Sequential pictures during tension deformation. (C) Measured force and related energy versus displacement. The bistable transition generates an energy barrier $\Delta U_2$ at the second equilibrium.

**(4) Measurement of the structural force of BOS with regulator**

The same experimental setup is used to measure structural forces on the BOS with regulator. One end of the regulator is secured to a corner of the BOS pentagon plate, while the opposite end passes through a base plate mounting hole. A steel caliper is fixed to the base plate serves as the measurement reference. During testing, predetermined prestrain is applied by stretching the regulator to align with the caliper's target scale. Final positioning of the regulator is maintained using two mechanical clamps.

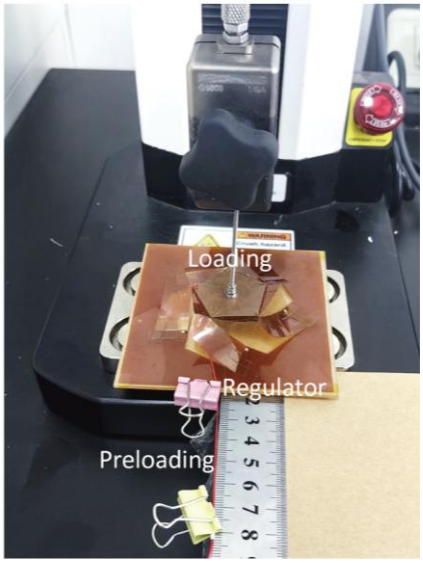


**Fig. S7.** Measurement of force of the BOS with regulator.

**(5) Measurement of the actuation force of BOS with thermal actuators**

To measure thermal actuation forces across temperatures, the BOS is equipped with a heater, five thermal actuators, and a thermocouple. The testing machine operates in position-holding mode, lowering the BOS to a predetermined height $\delta$ and taring the force sensor. A constant 5V voltage is applied to the heater while force-time and temperature-time profiles are synchronously recorded. Force-temperature curves are generated by cross-referencing the time-synchronized datasets. This procedure is repeated for multiple displacement setpoints $\delta$ to characterize the temperature-dependent force response.

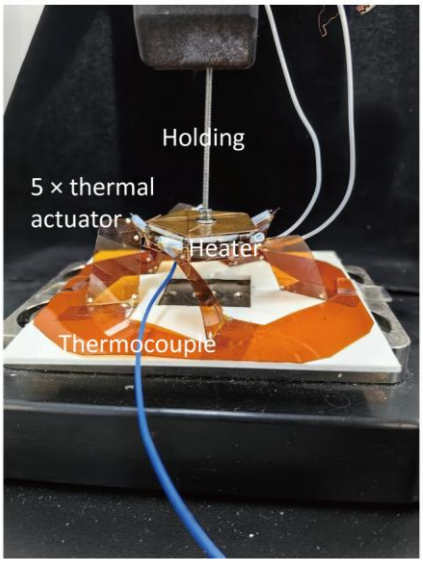


**Fig. S8.** Measurement of actuation force of the BOS with thermal actuators. The test machine is set to the holding mode. The temperature of the heater is recorded by thermocouple.

To obtain the actuation force-displacement curve of the BOS at 25°C, we first measure the force-displacement curve of the BOS with thermal actuators at 25°C, then subtract the baseline structural response without thermal actuators.

**Supplementary Note 4: Measurement of heat conductance**

The thermal characterization of the bistable origami switch (BOS) is conducted using a custom-built testing platform (Fig. 2A and Fig. S9), designed in accordance with ASTM-5470 standards. Measurements are conducted inside a sealed aluminum vacuum chamber under high-vacuum conditions of ~$10^{-3}$ Pa. The setup consists of two vertically aligned

stainless steel reference bars (20×20×50 mm) with precision-ground surfaces (Ra ≤ 0.025) to minimize radiation losses. The lower bar is fixed to the chamber base, while both bars are instrumented with three T-type thermocouples (±10 mK accuracy, 254 μm diameter) spaced 15 mm apart to record temperature gradient. Temperature data is recorded by two YET-640X four-channel thermometers. The BOS sample is tightly aligned between the reference bars using press-fit assembly, ensuring flush contact with the bar ends for efficient thermal coupling. An alumina-based ceramic heater is mounted on the top surface of the upper reference bar to provide a controlled heat input. For OFF-state measurements, the upper bar is suspended using nylon threads to eliminate contact (Fig. S9A). For ON-state measurements, it is lowered into direct contact with the lower bar (Fig. S9B). To enhance interfacial thermal conductance, a thin (~100 μm) layer of Apiezon H high-vacuum grease is applied at the contact interface.

The thermal conductance of the BOS in ambient air is measured using the same experimental platform and protocol as in vacuum conditions, with two key procedural modifications. First, the vacuum chamber is vented to atmospheric pressure (1 atm) while maintaining a hermetically sealed environment. Second, the thermal interface material (TIM) is changed. For vacuum measurements, a low-vapor-pressure TIM (Apiezon H) with a relatively low thermal conductivity of 0.216 W/m·K is used to avoid outgassing. In contrast, air-based measurements allow the use of high-performance TIMs, such as Shin-Etsu X-23-7921-5, a commercially available thermal grease with a significantly higher

thermal conductivity (>6 W/m·K), thereby minimizing interfacial thermal resistance.

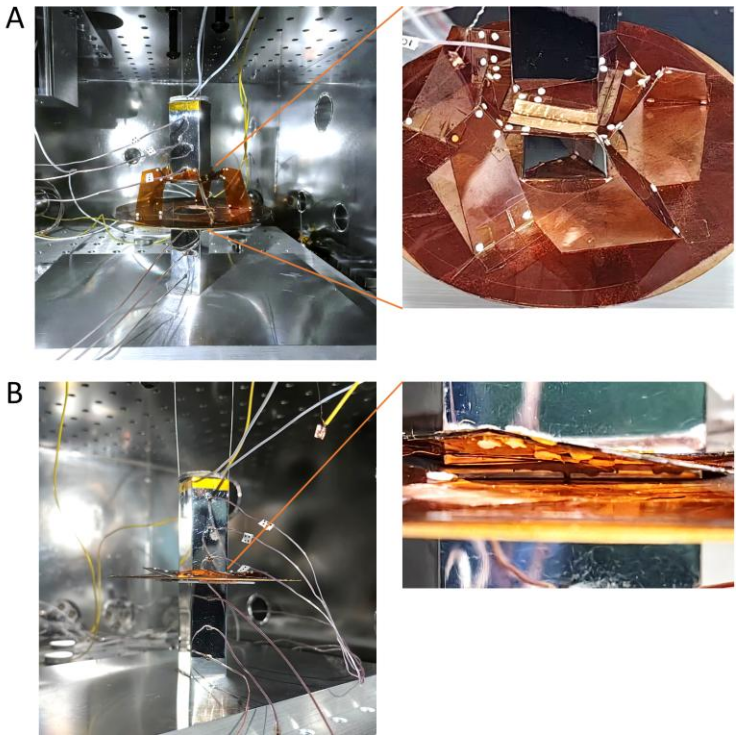


**Fig. S9.** Photo of the experimental set-up of two reference bars in a high-vacuum chamber at (A) OFF and (B) ON states.

It is noteworthy that thermal radiation losses along the reference bars are proportional to the fourth power of local temperature, resulting in slight non-uniformities in vertical heat flux. Due to its closer proximity in temperature to the ambient environment, the lower reference bar experiences reduced radiative loss and more closely satisfies the assumption of a linear temperature distribution. Therefore, the temperature gradient used to compute thermal conductance via Fourier's law $G = Q/\Delta T$ is obtained from a linear fit of the

temperature distribution along the lower bar. Detailed temperature distributions, extracted thermal conductance values, and corresponding switching ratios under vacuum conditions are presented and discussed in the main text.

**Supplementary Note 5: Thermal switching ratio of the bistable origami metastructure in air**

We further characterize the thermal conductance ($G_{on}$, $G_{off}$) and the thermal switching ratio, $\rho$, of the BOS under ambient air conditions. Temperature–time profiles recorded by six thermocouples for both ON and OFF states are presented in Fig. S10A-B. The corresponding spatial temperature distributions along the reference bars under steady-state conditions are shown in Fig. S10C-D. The results indicate that the OFF-state thermal behavior is strongly affected by ambient heat transfer mechanisms Specifically, parasitic heat losses due to air conduction and natural convection lead to energy dissipation from the upper reference bar before reaching the BOS. This diverted heat flux results in an asymmetric temperature profile between the upper and lower bars. Consequently, estimating the off-state thermal conductance $G_{off}$ using the temperature gradient from only one reference bar (either upper or lower) may significantly overestimate or underestimate the actual thermal conductance of the BOS under ambient conditions.

To ensure accurate assessment of the BOS's effective thermal conductance, we follow the ASTM-5470 standard methodology. Temperature gradients along both reference bars

are independently extracted via linear fitting and subsequently averaged to determine the net one-dimensional heat flux used in $G = Q/\Delta T$. Under otherwise identical conditions, the measured ON-state thermal conductance $G_{on}$ in air reaches 51685 W/m²·K, while the OFF-state conductance $G_{off}$ is determined to be 38 W/m²·K, markedly higher than the corresponding vacuum value of 2 W/m²·K. This increase is attributed to the additional heat transfer pathways introduced by air, including both conduction and natural convection. The resulting thermal switching ratio in ambient conditions is thereby calculated to be 1360.

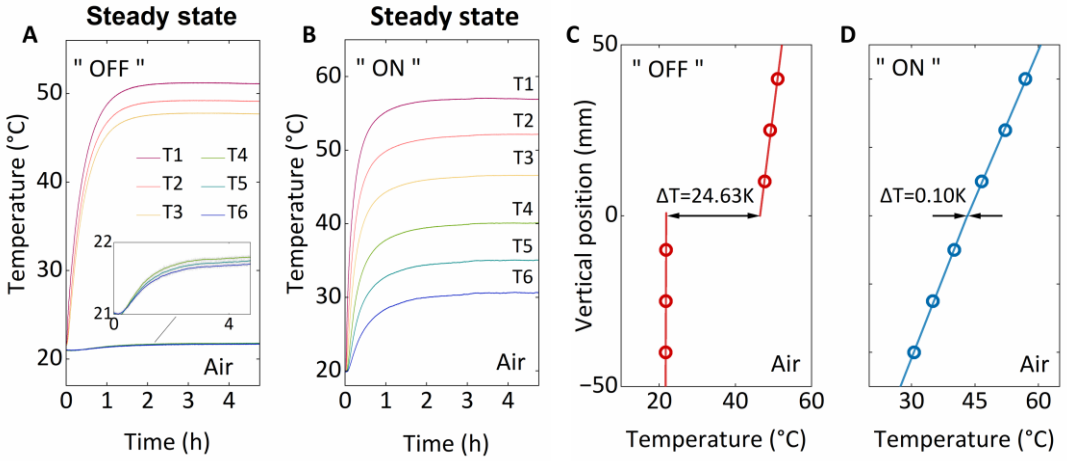


**Fig. S10.** (A, B) The temperature-time profiles recorded by the six thermocouples in the ON and OFF states under air. (C, D) Steady-state temperature distributions along the bars for the ON/OFF states under air. Interfacial temperature discontinuities are determined via linear extrapolation of bar temperatures.

**Supplementary Note 6: Model prediction of thermal conductance from reference bar experiments**

(1) Thermal Analysis under Vacuum

To enable a more rigorous interpretation of the reference bar measurements, we develop a simplified one-dimensional steady-state thermal conduction model. In the OFF state under vacuum conditions, heat transfer occurs primarily through two mechanisms: solid-state conduction and thermal radiation.

Given the geometric and material complexity of the BOS conduction path, several simplifying assumptions are made: (1) heat transport through the BOS is considered as a one-dimensional, steady-state conduction process; (2) the copper sheets in contact with the reference bars are assumed be isothermal. Although the copper layers are thermally in series with the BOS, their thermal resistances are orders of magnitude smaller than that of the polyimide structural elements and are therefore neglected; (3) interfacial contact resistances are omitted due to the substantial uncertainties associated with their theoretical estimation.

Based on these assumptions, the equivalent thermal resistance network for solid-state conduction in the OFF state is schematically depicted in Fig. S11.

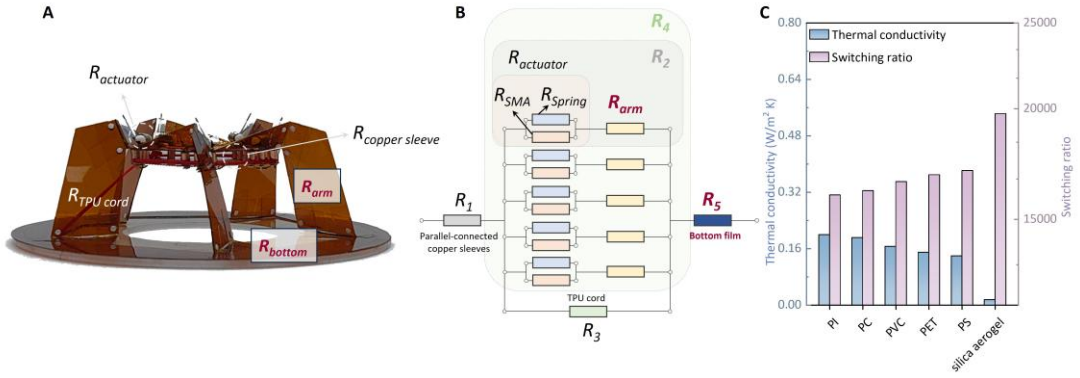


**Fig. S11. Base-material dependence of the BOS switching ratio. A~B**, Schematic illustration of the thermal-resistance network for solid-state heat conduction in the BOS under vacuum in the OFF state. **C,** Thermal conductivity and the corresponding switching ratio for representative base materials (PC, PVC, PET, PS, and silica aerogel).

This network comprises the following components:

$R_1$: Thermal resistance of the copper sleeves;

$R_2$: Series thermal resistance of a single thermal actuator and its corresponding PI arm;

$R_3$: Thermal resistance of the TPU elastic cord;

$R_4$: Effective thermal resistance of five identical arms (each with $R_2$) and one TPU elastic cord ($R_3$) connected in parallel;

$R_5$: Thermal resistance of the bottom PI film.

All thermal resistances are normalized by the effective thermal interface area $S_{int}$. The estimated resistance values employed in the model are summarized in Table S1.

**Table S1.** Estimated thermal resistance values and corresponding calculation details used in the OFF-state conduction model. All resistances are normalized by the effective thermal interface area $S_{int}$.

| **Thermal Resistor** | **Thermal Resistance (mm²·K/W)** | **Calculation Details** |
|---|---|---|
| $R_1$: Thermal Resistance of Copper Sleeves | 66.15 | Dimensions:<br>Inner radius: $r_{in} = 0.5$ mm<br>Outer radius: $r_{out} = 1.1$ mm<br>Height: $L_{copper\ sleeve} = 3$ mm<br>Cross-sectional area per sleeve:<br>$S_{sleeve} = \pi \cdot (r_{out}^2 - r_{in}^2) \approx 3.016\ \text{mm}^2$<br>Thermal conductivity of copper:<br>$\kappa_{copper} = 401\ \text{W/m} \cdot \text{K}$<br>Total resistance from 15 sleeves:<br>$R_1 = \frac{L_{sleeve} \cdot S_{int}}{15 \cdot \kappa_{copper} \cdot S_{sleeve}} \approx 66.15\ \text{mm}^2 \cdot \text{K/W}$ |
| $R_2$: Thermal Resistance of a Single Origami Arm | $1.37\times10^7$ | 1. Thermal Actuator (SMA + Spring in parallel):<br>(1) SMA Wire:<br>Length: $L_{SMA} = 17.5$ mm<br>Cross-sectional area: $S_{SMA} = \pi \cdot r_{SMA}^2 \approx 0.20\ \text{mm}^2$<br>Thermal conductivity(3): $\kappa_{SMA} \approx 10\ \text{W/m} \cdot \text{K}$ |

| | | |
|---|---|---|
| | | $R_{SMA} = \frac{L_{SMA} \cdot S_{int}}{\kappa_{SMA} \cdot S_{SMA}} \approx 3.50 \times 10^6\ \text{mm}^2 \cdot \text{K/W}$<br><br>(2) Spring:<br><br>Equivalent length: $L_{spring} = 3.6\ \text{mm}$<br><br>Inner radius: $r_{in} = 1.1\ \text{mm}$<br><br>Outer radius: $r_{out} = 1.5\ \text{mm}$<br><br>Cross-sectional area:<br><br>$S_{spring} = \pi \cdot (r_{out}^2 - r_{in}^2) \approx 3.27\ \text{mm}^2$<br><br>Thermal conductivity(4): $\kappa_{spring} \approx 16\ \text{W/m} \cdot \text{K}$<br><br>$R_{spring} = \frac{L_{spring} \cdot S_{int}}{\kappa_{spring} \cdot S_{spring}} \approx 2.75 \times 10^4\ \text{mm}^2 \cdot \text{K/W}$<br><br>(3) Combined thermal actuator resistance:<br><br>$R_{actuator} = \frac{1}{(\frac{1}{R_{SMA}} + \frac{1}{R_{spring}})} \approx 2.73 \times 10^4\ \text{mm}^2 \cdot \text{K/W}$<br><br>2. Polyimide Arm:<br><br>Length:<br><br>$L_{arm,PI} = \sqrt{a^2 + b^2 - 2ab\cos\alpha_1} \approx 22.65\ \text{mm}$<br><br>Cross-sectional area: $S_{arm,PI} \approx 3.3\ \text{mm}^2$<br><br>Thermal conductivity(5): $\kappa_{PI} \approx 0.20\ \text{W/m} \cdot \text{K}$<br><br>$R_{arm,PI} = \frac{L_{arm,PI} \cdot S_{int}}{\kappa_{PI} \cdot S_{arm,PI}} \approx 1.37 \times 10^7\ \text{mm}^2 \cdot \text{K/W}$<br><br>3. Total resistance of one arm:<br><br>$R_2 = R_{actuator} + R_{arm,PI} \approx 1.37 \times 10^7\ \text{mm}^2 \cdot \text{K/W}$<br><br>( $R_{actuator} \ll R_{arm,PI}$ ) |

| | | |
|---|---|---|
| $R_3$: Thermal Resistance of the TPU elastic cord | $1.50\times10^8$ | Length: $L_{TPU\ cord} = 45\ \text{mm}$<br>Cross-sectional area:<br>$S_{TPU\ cord} = \pi \cdot r_{TPU\ cord}^2 \approx 0.50\ \text{mm}^2$<br>Thermal conductivity: $\kappa_{TPU} \approx 0.2393\ \text{W/m} \cdot \text{K}$<br>$R_3 = \frac{L_{TPU\ cord} \cdot S_{int}}{\kappa_{TPU} \cdot S_{TPU\ cord}} \approx 1.50 \times 10^8\ \text{mm}^2 \cdot \text{K/W}$ |
| $R_4$: Parallel Combination of Five Arms and One TPU elastic cord | $2.69\times10^6$ | $R_4 = \frac{1}{(\frac{5}{R_2} + \frac{1}{R_3})} \approx 2.69 \times 10^6\ \text{mm}^2 \cdot \text{K/W}$ |
| $R_5$: Thermal Resistance of the Bottom PI Film | 156.43 | Thickness: $L_{bottom,PI} = 0.2\ \text{mm}$<br>Cross-sectional area: $S_{bottom,PI} \approx 2557\ \text{mm}^2$<br>$R_5 = \frac{L_{bottom,PI} \cdot S_{int}}{\kappa_{PI} \cdot S_{bottom,PI}} \approx 156.43\ \text{mm}^2 \cdot \text{K/W}$ |

As evident from the detailed calculations presented in Table S1, the thermal resistances of the SMA wire, the spring, and the TPU cord contribute negligibly to the total thermal resistance network—being significantly smaller than that of the low-thermal-conductivity polyimide structural components. This observation justifies the exclusion of these elements in the actual reference bar experiments.

Accordingly, the contribution of solid-state conduction to the OFF state thermal conductance under vacuum conditions can be expressed as:

$$G_{off-conduction} = \frac{1}{R_1 + R_4 + R_5} \approx 0.37\ \mathrm{W/m^2 \cdot K} \tag{S14}$$

The second heat transfer pathway in the OFF state is thermal radiation between two opposing surfaces held at different temperatures. The upper surface comprises a copper sheet, while the lower surface corresponds to the stainless-steel reference bar, coated with thermal interface material. Based on literature-reported values(6, 7), the emissivity of the respective surfaces is assumed to be:

$$\varepsilon_1 \approx 0.2\ (copper)$$

$$\varepsilon_2 \approx 0.75\ (\mathrm{TIM-coated\ stainless\ steel})$$

From the temperature data shown in Fig. 2D (left), the surface temperatures are approximated as $T_1$=66.57℃, $T_2$=24.70℃. The net radiative heat flux is computed using the Stefan–Boltzmann law:

$$q_{rad} = \frac{\sigma \cdot (T_1^4 - T_2^4)}{\frac{1}{\varepsilon_1} + \frac{1}{\varepsilon_2} - 1} \approx 57.93\ \mathrm{W/m^2} \tag{S15}$$

where $\sigma = 5.67 \times 10^{-8}\ \mathrm{W/m^2 \cdot K^4}$ is the Stefan–Boltzmann constant. The

corresponding radiative thermal conductance is then:

$$G_{off-radiation} = \frac{q_{rad}}{\Delta T} \approx 1.38\ \mathrm{W/m^2 \cdot K} \tag{S16}$$

Combining both the solid conduction and radiation contributions, the calculated total OFF state thermal conductance under vacuum is given by:

$$G_{off} = G_{off-conduction} + G_{off-radiation} \approx 1.75\ \mathrm{W/m^2 \cdot K} \tag{S17}$$

In the ON state, thermal contact is established directly between the top and bottom reference bars *via* a high-performance TIM layer. Since neither the interfacial thermal resistance nor the TIM layer thickness can be reliably determined analytically, we adopt the experimentally measured value: $G_{on} = 27968\ \mathrm{W/m^2 \cdot K}$. Thus, the predicted thermal switching ratio under vacuum is:

$$\rho_{vacuum} = \frac{G_{on}}{G_{off}} \approx 15982 \tag{S18}$$

It is important to emphasize that the model-predicted solid conduction contribution $G_{off-conduction} \approx 0.37\mathrm{W/m^2 \cdot K}$ should be interpreted as an upper bound, as it neglects all interfacial contact resistances. The discrepancy between the theoretical switching ratio

$\rho_{vacuum}$ and its experimentally measured value likely arises from uncertainties in the estimation of surface emissivities, which directly influences the radiative heat transfer component.

(2) Comparison of the $G_{off}$ in vacuum between this work and other contact-based thermal switches

For the SMA–spring thermal regulator designed by Hao et al.(8), the OFF state thermal conductance $G_{off}$ was experimentally measured using a reference bar setup to be 1.13 W/m²·K, while thermal modeling predicted a range of 0.94–1.25 W/m²·K. However, it is important to note that both the experimental and modeling approaches omitted the parallel solid conduction contribution from the metallic spring component, a critical component of the regulator. Specifically, in the reference bar experiment, the spring was placed beneath the lower bar to mechanically actuate separation between the bars, thereby isolating it from the thermal conduction path and excluding its contribution from the measured $G_{off}$.

Nevertheless, the spring is an essential functional element of thermal regulation mechanism; without its action, the system would not exhibit switching behavior. In practical thermal management scenarios, the SMA and spring operate in tandem as an integrated unit—an arrangement reflected in the authors' own demonstration setup and explicitly accounted for in the thermal resistance network used in their battery experiment.

Based on the reported geometry, thermal conductivity, quantity, and connection configuration of the SMA and spring components in the battery experiment, their respective thermal conductance contributions (normalized to the effective thermal interface area $A_{area}$ used in the reference bar test) are estimated as follows:

① SMA wire:

Length: $L_{SMA} \approx 0.025$ m

Cross-sectional area per wire:

$$S_{SMA} = \pi \cdot r_{SMA}^2 \approx \pi \cdot (127\mu m)^2 \tag{S19}$$

Thermal conductivity: $\kappa_{SMA} \approx 10\ \mathrm{W/m \cdot K}$

Thermal resistance (4 wires in parallel):

$$R_{SMA} = \frac{L_{SMA} \cdot A_{area}}{4 \cdot \kappa_{SMA} \cdot S_{SMA}} \tag{S20}$$

Thermal conductance: $G_{SMA} \approx 0.20\ \mathrm{W/m^2 \cdot K}$

② Spring:

Length: $L_{Spring} \approx 0.05$ m

Cross-sectional area per spring:

$$S_{Spring} = \pi \cdot r_{Spring}^2 \approx \pi \cdot (500\mu m)^2 \tag{S21}$$

Thermal conductivity: $\kappa_{Spring} \approx 16\ \mathrm{W/m \cdot K}$

Thermal resistance (5 springs in parallel):

$$R_{Spring} = \frac{L_{spring} \cdot A_{area}}{5 \cdot \kappa_{spring} \cdot S_{spring}} \tag{S22}$$

Thermal conductance: $G_{Spring} \approx 3.14\ \mathrm{W/m^2 \cdot K}$

Therefore, the total solid conduction contribution is:

$$G_{off-conduction} = G_{SMA} + G_{Spring} \approx 3.34\ \mathrm{W/m^2 \cdot K} \tag{S23}$$

The radiative heat transfer contribution, as reported by the authors, is:

$$G_{off-radiation} \approx 0.64\ \mathrm{W/m^2 \cdot K} \tag{S24}$$

Accordingly, the total OFF state thermal conductance of the SMA–spring thermal regulator is estimated as:

$$G_{off} = G_{off-conduction} + G_{off-radiation} \approx 3.98\ \mathrm{W/m^2 \cdot K} \tag{S25}$$

(3) Model-Predicted Design Space for the BOS Switching Ratio

The bistable origami architecture offers tunable geometric parameters—including arm length $L_{arm}$, arm width $W_{arm}$, and lift height $\delta$—thereby enabling a versatile design space and a correspondingly wide range of thermal switching ratios. Under vacuum conditions, the only geometry-dependent term in the overall thermal resistance network (as listed in Table S1) is the resistance of the polyimide arms, while all other resistances are treated as constants. The PI-arm thermal resistance can be expressed as:

$$R_{arm} = \frac{L_{arm} \cdot S_{int}}{\kappa_{PI} \cdot W_{arm} \cdot t} \tag{S26}$$

where $\kappa_{PI}$ is the thermal conductivity and $t$ is the thickness of the arm. By systematically scanning over a parameter space defined by $W_{arm} = 15 - 21.5\ \mathrm{mm}$, $L_{arm} = 21 - 28.6\ \mathrm{mm}$, and $\delta = 16 - 26.3\ \mathrm{mm}$, we compute the corresponding OFF state thermal conductance $G_{off}$, forming the design space illustrated in Fig. S12. Using the experimentally measured ON state conductance $G_{on} = 27968\ \mathrm{W/m^2 \cdot K}$, the resulting switching-ratio distribution under vacuum is plotted in the main text as Fig. 2G

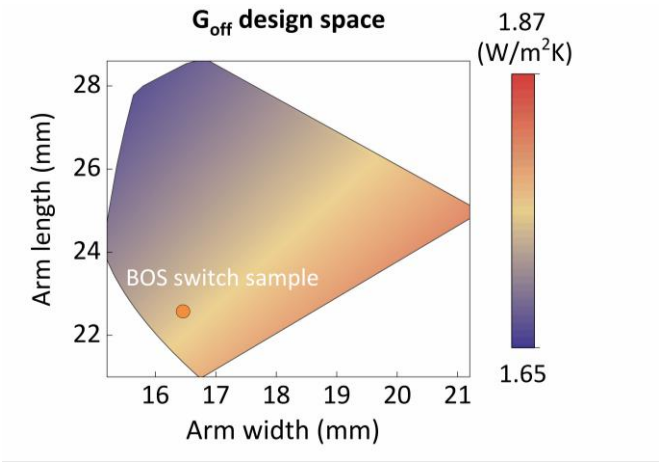


**Fig. S12.** Theoretical thermal conductance in OFF state ($G_{off}$), showing the dependence of the $G_{off}$ on arm width and length.

These results highlight the inherent geometric tunability of the origami-based switch, which enables precise and extensive control over its thermal transport behavior. The broad and continuous adjustability in thermal switching ratio demonstrates not only the platform's strong switching performance, but also its high scalability, and potential for integration into advanced thermal management systems.

**Supplementary Note 7: Folding behavior of the bistable origami structure**

The folding process of the BOS involves five kinematic parameters $\{\delta, \theta, \gamma_1, \gamma_2, \gamma_3\}$ (Fig. S13). $\delta$ and $\theta$ represent the vertical displacement and rotation angle of the central plate, respectively. Parameters $\gamma_1$, $\gamma_2$, and $\gamma_3$ correspond to twisting angles about the three creases. Crucially, $\gamma_1$, $\delta$ and $\theta$ derive from rigid-body motion and can be modeled

kinematically under the rigid folding assumption(9). These parameters are governed by the rotation of edge $A_1B_1$ about crease $B_1C_0$, which mechanically constrains the origami structure to a deterministic folding trajectory. In contrast, $\gamma_2$ and $\gamma_3$ reflect incompatible folding(10) induced by arm panel deformation, directly enabling the bistable mechanism.

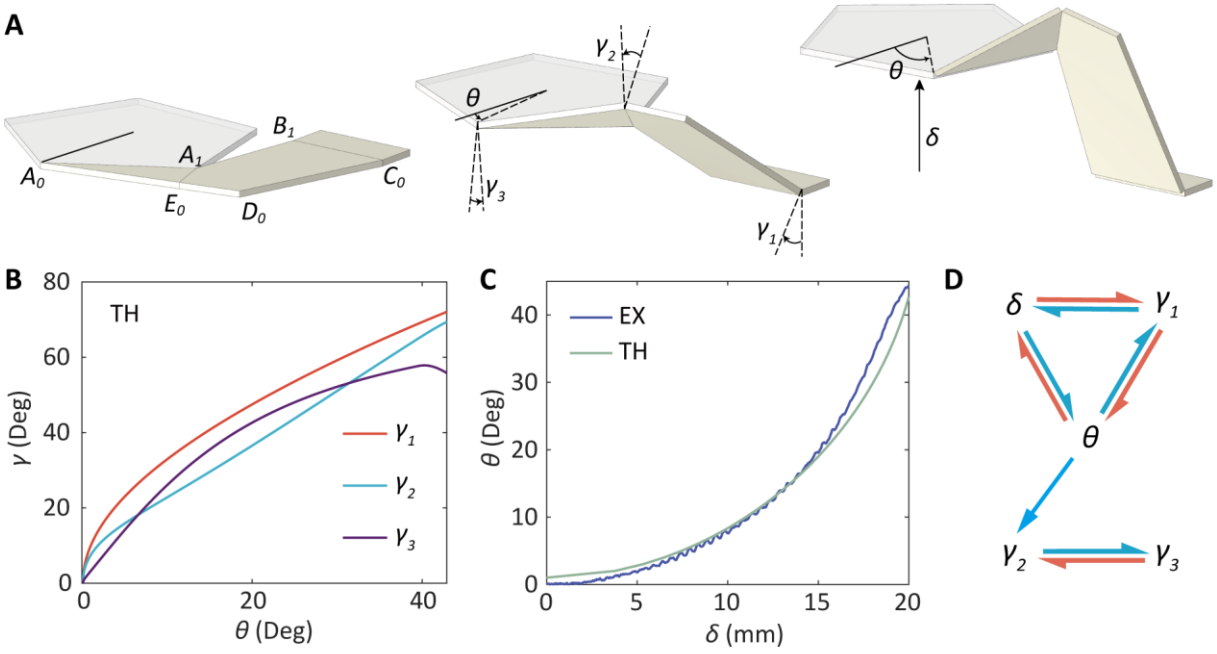


**Fig. S13.** (A) Folding sequence of the three-crease arm from flatten state to standing state. (B) Folding angles $\gamma_1$, $\gamma_2$, and $\gamma_3$ are a function of the hub rotation angle $\theta$. (C) Pentagon plate rotation angle $\theta$ is a function of the arm standing distance $\delta$. (D) Five kinematic parameters $\{\delta, \theta, \gamma_1, \gamma_2, \gamma_3\}$ are interdependently constrained.

Using arm segment $A_0A_1B_1C_0D_0$ as a representative case, we establish a kinematic model describing the BOS's motion. This model parameterizes the arm's deformation

through vertex displacements and hinge rotations.

(1) Relationship between $\gamma_1$, $\delta$, and $\theta$

Assuming that the length of $A_1B_1$ remains constant during deformation, the length of $A_1B_1$ in the flat state is given by:

$$L_{A_1B_1} = \|A_1B_1\| = \sqrt{a^2 + b^2 - 2ab\cos\alpha_1} \tag{S27}$$

During the folding process, the coordinate of point $A_0$ and $A_1$ becomes:

$$\begin{aligned} A_0' &= (a\cos(\theta_0 - \alpha_1 + \theta), a\sin(\theta_0 - \alpha_1 + \theta), \delta) \\ A_1' &= (a\cos(\theta_1 - \alpha_1 + \theta), a\sin(\theta_1 - \alpha_1 + \theta), \delta) \end{aligned} \tag{S28}$$

The length of $A_1'B_1$ is calculated by:

$$L_{A_1'B_1} = \|A_1'B_1\| = \sqrt{a^2 + b^2 - 2ab\cos(\alpha_1 - \theta) + \delta^2} \tag{S29}$$

Using the length equivalence $L_{A_1B_1} = L_{A_1'B_1}$, we derive the following relationship:

$$\delta = \sqrt{2ab(\cos(\alpha_1 - \theta) - \cos\alpha_1)} \tag{S30}$$

The distance from point $A_1'$ to edge $B_1C_0$ is calculated using the area method as:

$$d = \frac{\overrightarrow{B_1C_0} \times \overrightarrow{B_1A_1}}{\|B_1C_0\|} = \frac{|a^2\cos(\alpha_1+\alpha_2+\theta+\frac{\pi}{10}) + ab(\sin(\alpha_1+\theta) - \cos(\alpha_2+\frac{\pi}{10}))|}{\sqrt{a^2+b^2-2ab\sin(\alpha_2+\frac{\pi}{10})}} \tag{S31}$$

The twisting angle $\gamma_1$ could be obtained from the trigonometric function relationship

$$\gamma_1 = \sin^{-1}(\delta/d) \tag{S32}$$

(2) Relationship between $\gamma_2$, $\gamma_3$ and $\theta$

$\gamma_2$ and $\gamma_3$ are governed by $\theta$ and arm deformation. Under rigid folding constraints where $E_0$ rotates about hinge $A_1A_0$ while $D_0$ rotates about hinge $E_0A_1$, we partially define their motion. First analyzing point $E_0$, its displacement results from two sequential transformations: rigid translation with the pentagon plate during its $\theta$ rotation and $\delta$ lift, followed by $\gamma_3$ rotation about hinge $A_1'A_0'$. The coordinate transformation for $E_0$ through rotation $\theta$ and vertical displacement $\delta$ is given by:

$$E_0' = \begin{bmatrix} E_{0x}' \\ E_{0y}' \\ \delta \end{bmatrix} = \begin{bmatrix} \cos\theta & -\sin\theta & 0 \\ \sin\theta & \cos\theta & 0 \\ 0 & 0 & 1 \end{bmatrix} \begin{bmatrix} E_{0x} \\ E_{0y} \\ 0 \end{bmatrix} + \begin{bmatrix} 0 \\ 0 \\ \delta \end{bmatrix} \tag{S33}$$

When $E_0'$ rotates about hinge $A_1'A_0'$ by angle $\gamma_3$, the coordination of point $E_1'$ is

calculated via Rodrigues' rotation formula(11):

$$\frac{\overrightarrow{A_1'E_0''}}{\|A_1E_0\|} = \cos\gamma_3 \frac{\overrightarrow{A_1'E_0'}}{\|A_1E_0\|} + (1-\cos\gamma_3)\left(\frac{\overrightarrow{A_1'A_0'}}{\|A_1A_0\|}\cdot\frac{\overrightarrow{A_1'E_0'}}{\|A_1E_0\|}\right)\frac{\overrightarrow{A_1'A_0'}}{\|A_1A_0\|} + \sin\gamma_3\left(\frac{\overrightarrow{A_1'A_0'}}{\|A_1A_0\|}\times\frac{\overrightarrow{A_1'E_0'}}{\|A_1E_0\|}\right) \tag{S34}$$

Here, the coordinate of $E_0''$ depends on $\gamma_3$, making hinge $A_1'E_0''$ a function of $\gamma_3$. We analyze the position of $D_0$ through sequential transformations: First, it rigidly translates with $E_0$, then rotates about hinge $A_1'E_0''$. At the first step, the position of $D_0$ lies along the extending line of $A_0'E_0''$:

$$D_0'' = E_0'' + \frac{\overrightarrow{A_0'E_0''}}{\|A_0E_0\|}\|E_0D_0\| \tag{S35}$$

Next, the position of point $D_0''$ after rotation about hinge $A_1'E_0''$ by angle $\gamma_2$ is calculated using Rodrigues' rotation formula:

$$\frac{\overrightarrow{E_1'D_1'''}}{\|E_1D_1\|} = \cos\gamma_2 \frac{\overrightarrow{E_1'D_1''}}{\|E_1D_1\|} + (1-\cos\gamma_2)\left(\frac{\overrightarrow{A_1'E_1''}}{\|A_1E_1\|}\cdot\frac{\overrightarrow{E_1'D_1''}}{\|E_1D_1\|}\right)\frac{\overrightarrow{A_1'E_1''}}{\|A_1E_1\|} + \sin\gamma_2\left(\frac{\overrightarrow{A_1'E_1''}}{\|A_1E_1\|}\times\frac{\overrightarrow{E_1'D_1''}}{\|E_1D_1\|}\right) \tag{S36}$$

Here, the coordinate of $E_0''$ depends on both $\gamma_2$ and $\gamma_3$. At this stage, we have established all kinematic relationships governing the BOS's folding behavior. However, $\gamma_2$ and $\gamma_3$ remain undetermined and these will be resolved through the energy model in the following analysis.

**Supplementary Note 8: Theoretical modelling of the bistable origami structure**

The potential energy of the BOS originates from crease folding energy and arm panel bending energy. Pentagon plate rotation induces arm length changes that generate compressive forces, enabling bistability. Within the coordinate frame, an energy model is established from vertex coordinate variations(12, 13). Two assumptions are made below:

1. All the creases ($B_1C_0$, $A_1E_0$, $A_0A_1$, et al.) undergo rigid folding.

2.The central pentagon plate and triangle arm panels (e.g., $A_0A_1E_0$) remain rigid.

Thus, we calculate only the folding energy $U_{\gamma1}$, $U_{\gamma2}$, and $U_{\gamma3}$ (creases $B_1C_0$, $A_1E_0$, and $A_0A_1$), and the bending energy of the arm $U_{b1}$ and $U_{b2}$ (horizontal and vertical directions). The membrane energy is neglected due to negligible strain.

(1) Folding energy

The folding energy of each crease is expressed as(14)

$$U_\gamma = \frac{1}{2} k_\gamma l_\gamma (\Delta\gamma)^2 \tag{S37}$$

where $k_\gamma$ is the rotational stiffness, $l_\gamma$ is the length of creases, and $\Delta\gamma$ is the folding angle.

(2) Bending energy

Bending deformation predominantly occurs in panel $B_1C_0D_0E_0A_1$. To analyze bending energy, this panel is modeled as a beam. Based on Timoshenko beam theory, the buckling deformation can be represented as a Fourier sine series:

$$y = a_1 \sin\frac{\pi x}{l} + a_2 \sin\frac{2\pi x}{l} + \cdots + a_n \sin\frac{n\pi x}{l} \tag{S38}$$

Here, $l$ represents the distance between the beam's endpoints, and $a_n$ denotes the amplitude coefficient of the sine function. To simplify the analysis, we retain only the first term of the series:

$$y = a_1 \sin\frac{\pi x}{l} \tag{S39}$$

The strain energy of a beam under bending is expressed as

$$U_b = \frac{EI}{2}\int_0^l \left(\frac{d^2y}{dx^2}\right)^2 dx = \frac{EI}{2}\left[a_1^2\frac{n^4\pi^4}{l^4}\sin^2\frac{\pi x}{l}\right]_0^l = a_1^2\frac{\pi^4 EI}{4l^3} \tag{S40}$$

To determine $a_1$, we apply the constraint that the beam's arc length equals its initial length $L$. The arc length integral is expressed as:

$$L = \int_0^l \sqrt{1+\left(\frac{dy}{dx}\right)^2}\,dx = \int_0^l \sqrt{1+\left(\frac{a_1\pi}{l}\cos\frac{\pi x}{l}\right)^2}\,dx \tag{S41}$$

According to the Taylor expansion formula, $\sqrt{1+u} = 1+\frac{1}{2}u-\frac{1}{8}u^2+\cdots$, the first two terms are selected for integration, as $u^2 = \left(\frac{a_1\pi}{l}\cos\frac{\pi x}{l}\right)^4 \approx 0$. Reducing the integral to:

$$L \approx \int_0^l 1+\frac{1}{2}\left(\frac{a_1\pi}{l}\cos\frac{\pi x}{l}\right)^2 dx = l+\frac{\pi^2 a_1^2}{4l} \tag{S42}$$

Rearranging for $a_1$, we get

$$a_1 = \frac{2}{\pi}\sqrt{l(L-l)} \tag{S43}$$

Substituting Eq. S43 into Eq. S40, we can get

$$U_b = \frac{\pi^2 EI}{l^2}(L - l) = \frac{\pi^2 EI}{l^2}\Delta l \tag{S44}$$

where $EI$ is the flexural rigidity and $I = \frac{bt^3}{12}$, $b$ is the beam width, $t$ is the thickness. $L$ is the total length of the beam, $l$ is the current end-to-end distance, $\Delta l$ represents the compression distance.

To validate the analytical model, comparisons are made with finite element simulations (Fig. S14). Horizontal loading applied at point $A_1$ produced asymmetric bending energy between positive and negative directions due to the adaptive selection of equivalent beam configurations. This directional dependency arises from the fundamental approach where points $A_1$, $B_1$, and $C_0$ are used to define either a rigid rod or equivalent beam depending on loading direction. Specifically,

the rigid rod forces rotation about end pivot. The roles of rigid rod and equivalent beam interchange based on force direction. Through rigid-body kinematics about these pivots, the instantaneous position of $A_1$ is determined, enabling calculation of the compressive displacement ($\Delta l$) and resulting bending energy.

For loading in the -x direction, $A_1C_0$ is defined as the equivalent beam while $A_1B_1$ serves as the rigid rod. When applying a displacement load of $-u_x$, the coordinate of point $A_1$ is

$$A_1' = \left( A_{1x} - u_x, B_{0y} + \sqrt{\left(A_{1y} - B_{0y}\right)^2 - 2u_x(A_{1x} - B_{0x}) - u_x^2} \right) \tag{S45}$$

The bending energy of the equivalent beam is

$$U_{b1}' = \frac{\pi^2 EI}{l_{A_1'C_0}^2} \Delta l_{A_1C_0} = \frac{\pi^2 EI}{\|A_1'C_0\|} (\|A_1C_0\| - \|A_1'C_0\|) \tag{S46}$$

Conversely, for loading in the +x direction, $A_1C_0$ serves as the rigid rod, while $A_1B_1$ is the equivalent beam. When applying a displacement load of $+u_x$, the coordinate of point $A_1$ is

$$A_1' = \left( A_{1x} - u_x, C_{0y} - \sqrt{\left(A_{1y} - C_{0y}\right)^2 - 2u_x(A_{1x} - C_{0x}) - u_x^2} \right) \tag{S47}$$

The bending energy of the equivalent beam is

$$U_{b1}'' = \frac{\pi^2 EI}{l_{A_1'B_1}^2} \Delta l_{A_1B_1} = \frac{\pi^2 EI}{\|A_1'B_1\|} (\|A_1B_1\| - \|A_1'B_1\|) \tag{S48}$$

When applying a vertical loading at point $D_0$, the compression of the panel is straightforward. $D_0C_0$ is defined as the equivalent beam. When applies a displacement

load of $u_y$, the coordinate of point $D_0$ is

$$D_0' = \left(D_{0x}, D_{0y} - u_y\right) \tag{S49}$$

The bending energy of the equivalent beam is

$$U_{b2} = \frac{\pi^2 EI}{l_{D_0'C_0}^2} \Delta l_{D_0C_0} = \frac{\pi^2 EI}{\|D_0'C_0\|} \left(\|D_0C_0\| - \|D_0'C_0\|\right) \tag{S50}$$

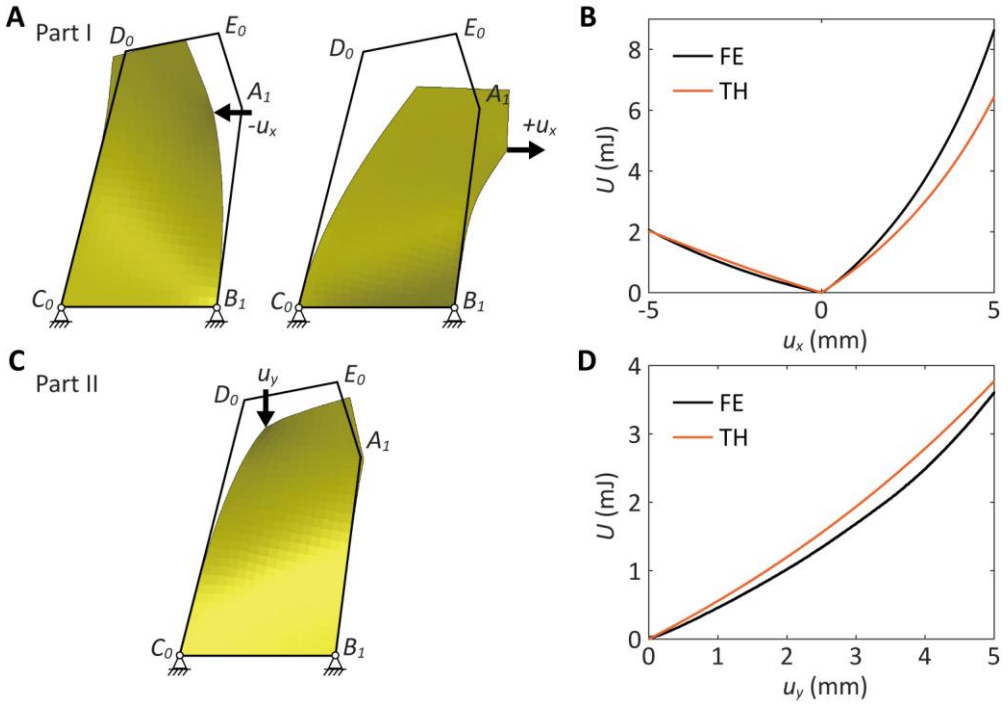


**Fig. S14.** Comparison of the bending energy of a single arm from finite element simulations and theoretical model subjected to unidirectional loading. ANSYS/LSDYNA 4-node Belytschko-Tsay shell elements are used in the finite element simulations. (A) For

horizontal loading, the bottom is fixed, and a displacement load is applied at point $A_1$ along the positive or negative direction. (B) Bending energy $U$ is a function of horizontal displacement $u_x$ and the energy is asymmetric along the positive and negative directions. (C) For vertical loading, the bottom is fixed, and a compressive displacement load is applied at point $D_0$. (D) Bending energy $U$ is a function of vertical displacement $u_y$.

(3) Total energy

The energy model for the bistable origami structure (Fig. S15) includes rigid plates, rigid rods, equivalent beams, and rotational hinges. The inner plate and triangle plates of the arms are set as rigid plates. The arm pentagon panels are simplified into a structural assembly composing of a rigid rod and two equivalent beams. All creases are defined as hinges. According to the deformation of the arm, the total energy is divided into two parts. The first part is from the rotation of the inner plate generating horizontal displacement load at point $A_1$, and simultaneous folding hinge $B_1C_0$. The energy of this part is expressed as

$$U_I = U_{\gamma 1} + U_{b1} = \frac{1}{2} k_\gamma l_{\gamma 1} (\Delta\gamma_1)^2 + \frac{\pi^2 EI}{l_{A_1C_2}^2} \Delta l_{A_1C_0} + \frac{\pi^2 EI}{l_{A_1B_2}^2} \Delta l_{A_1B_1} \tag{S51}$$

The second part involves folding hinges $A_1E_0$ and $A_0A_1$ coupled with vertical compression of the arm. The energy of this part is expressed as

$$U_{II} = U_{\gamma 2} + U_{\gamma 3} + U_{b2} = \frac{1}{2} k_\gamma l_{\gamma 2} (\Delta\gamma_2)^2 + \frac{1}{2} k_\gamma l_{\gamma 3} (\Delta\gamma_3)^2 + \frac{\pi^2 EI}{l_{D_0C_0}^2} \Delta l_{D_0C_0} \tag{S52}$$

The folding angles $\gamma_2$ and $\gamma_3$ are also determined here by minimizing the system's energy:

$$(\gamma_2, \gamma_3) = \arg\min_{\gamma_2, \gamma_3} U_{II} \tag{S53}$$

The total energy of the bistable origami structure synthesizes both energy in part I and II:

$$\begin{aligned} U = 5U_I + 5U_{II} = 5 \Big[ & \frac{1}{2} k_\gamma l_{\gamma 1} (\Delta\gamma_1)^2 + \frac{\pi^2 EI}{l_{A_1C_0}^2} \Delta l_{A_1C_0} + \frac{\pi^2 EI}{l_{A_1B_1}^2} \Delta l_{A_1B_1} + \\ & \frac{1}{2} k_\gamma l_{\gamma 2} (\Delta\gamma_2)^2 + \frac{1}{2} k_\gamma l_{\gamma 3} (\Delta\gamma_3)^2 + \frac{\pi^2 EI}{l_{D_0C_0}^2} \Delta l_{D_0C_0} \Big] \end{aligned} \tag{S54}$$

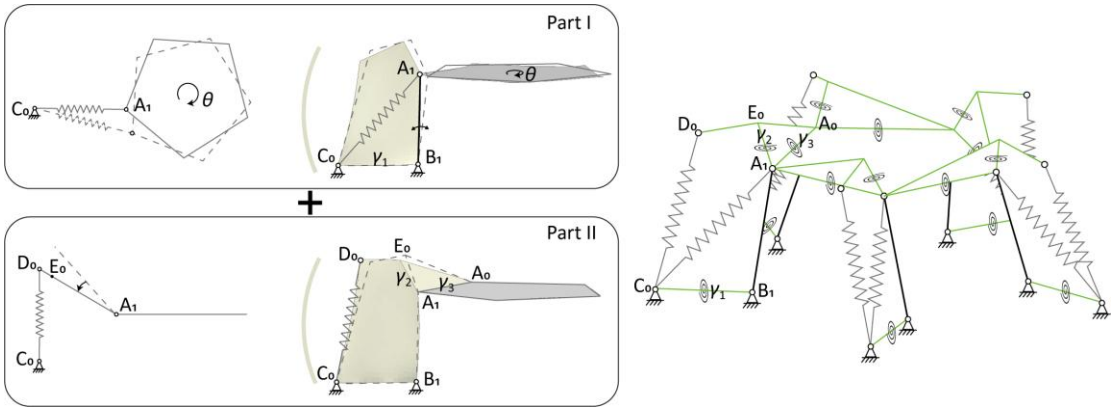


**Fig. S15.** Folding and bending behavior of BOS. The deformation of BOS includes two

parts: the deformation of arm caused by rotation of the pentagon (Part I) and the folding of hinges $A_1E_0$ and $A_0A_1$ with angles $\gamma_2$ and $\gamma_3$ (Part II). Both of them compress the arm elastically, and two spring are used to represent the deformation. Bar and hinge model for BOS.

Fig. S16 benchmarks the total energy predicted by the energy model against finite element simulations, while Fig. S18 compares theoretical predictions with experimental results across varying geometric parameter $\alpha_2$ (defined in Note 1). The energy model demonstrates strong agreement with both validation methods, confirming its accuracy in capturing bistable behavior.

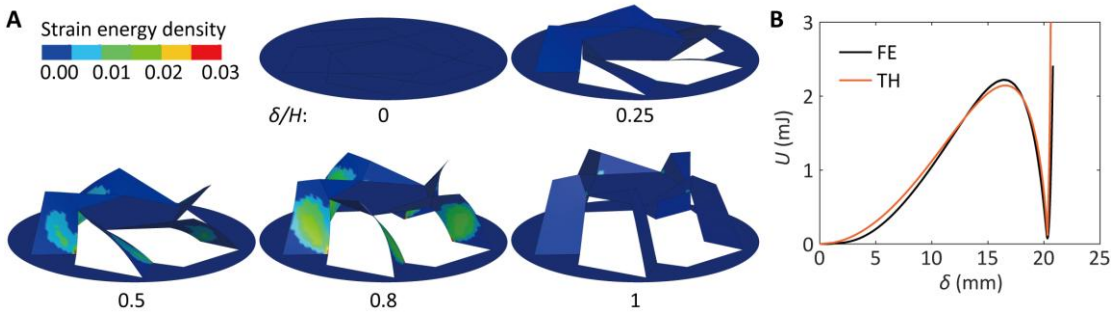


**Fig. S16.** Deformation and strain energy of a bistable origami structure during standing up. (A) Bending strain energy density from the finite element simulation. (B) Total energy versus vertical displacement.

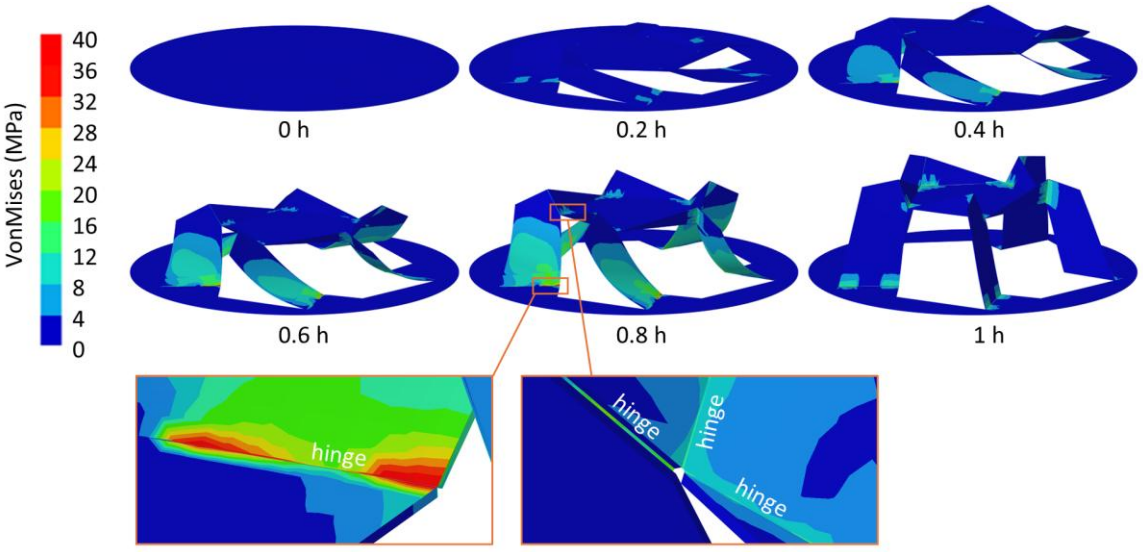


**Fig. S17.** Stress distribution of a bistable origami structure from the finite element simulation.

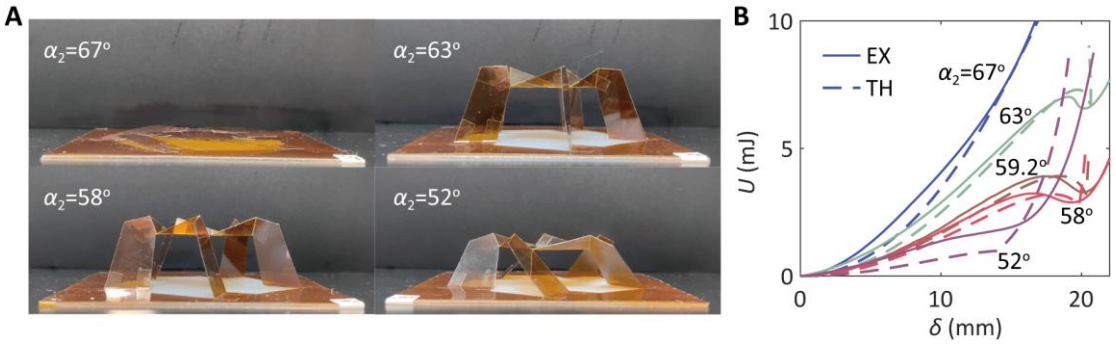


**Fig. S18.** Comparison of the total energy of bistable origami structures with different geometric design of $\alpha_2$. (A) Side views of experimental samples with $\alpha_2$ of 67°, 63°, 58° and 52°. The sample with $\alpha_2$ of 67° is restricted to rotate and can't stand up. (B) Total energy versus vertical displacement of those samples by experimental measurements and theoretical calculation.

**Supplementary Note 9: Analysis of the effect of geometric size on bistable properties**

Through the energy model, we establish the viable design space for BOS. A functional BOS requires confirmed bistability, which we investigated by altering $\alpha_1$, $\alpha_2$, and radius $b$ (Fig. S19A). With $a$ = 20 mm and $c$ = 40 mm held constant, and $b$ fixed at a nominal value $\hat{b}$ = 25 mm, we swept $\alpha_1$ and $\alpha_2$ within 42°-72°. These parameters are substituted into the energy model (Note 6) to generate potential energy landscapes.

Bistability emerges when $\Delta U_2 > 0$ – indicating an energy barrier between stable states – whereas monotonically increasing profiles signify monostability. The resulting phase diagram for fixed $\hat{b}$ (Fig. S19B) reveals three distinct behavioral regions within the ($\alpha_1$ and $\alpha_2$) parameter space. The central region exhibits bistable characteristics, with energy barrier $\Delta U_2$ decaying symmetrically toward the boundaries. Adjacent to this, an upper region shows monostable behavior where excessive $\alpha_1$ values induce prohibitive arm distortion, creating energy barriers that prevent full structural deployment. Conversely, the lower region demonstrates monostability through reduce arm distortion, as reduced $\alpha_2$ values allow deployment without bistable locking.

Next, we examine the influence of radius $b$ on bistability using phase diagrams (Fig. S19B-E). For $b$ ranging from 22–31 mm, systematic shifts in bistable behavior emerge. Decreasing $b$ from 25 mm to 22 mm reduces the energy barrier $\Delta U_2$ when $\alpha_2 > 60°$ while simultaneously shifting the bistable region downward toward smaller $\alpha_2$ values. Conversely, increasing $b$ to 28 mm or 31 mm shifts the bistable region upward toward

larger $\alpha_2$ and amplifies $\Delta U_2$. Geometrically, this compensation arises because reducing $b$ shortens the effective arm length, while smaller $\alpha_2$ elongates it – collectively maintaining arm length within a stable deformation range conducive to bistability.

Fig. S19F quantifies how radius $b$ influences bistability, comparing both the bistable area ratio and maximum energy barrier $\Delta U_2$. The nominal value $\hat{b} = 25$ mm maximizes the bistable design space while maintaining an optimal energy barrier for snap-through. Fig. S20 further illustrates the geometric structures of BOS within the ($\alpha_1$ and $\alpha_2$) parameter space: arm width is bounded between 15–21.5 mm, while standing height ranges from 16 to 26.3 mm across viable configurations.

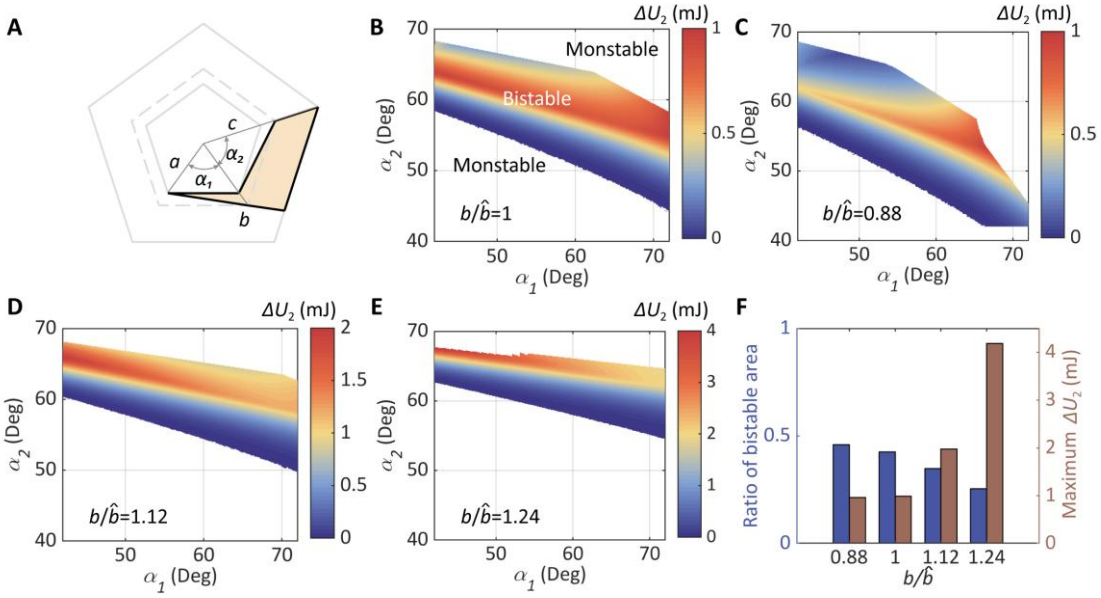


**Fig. S19.** Effect of geometric design on the bistable properties of the origami structure. (A) Schematic of the design parameters. The radius of the inner and outer pentagons ($a$ and $c$) is fixed as 20 and 40 mm. The radius of middle pentagon $b$ is initially set as $\hat{b}$ = 25 mm.

(B-E) Bistability phase diagram versus different $b$. (F) Comparison of bistable area ratio and max energy barrier under different $b$.

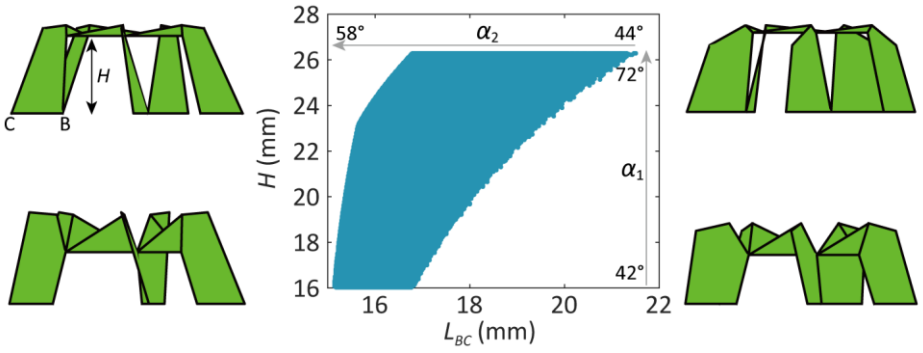


**Fig. S20.** Effect of geometric design on the width of arm $L_{BC}$ and standing height $H$.

**Supplementary Note 10: Analysis of effect of regulator on bistable origami metastructure**

The BOS exhibits a dimensional variation between elevated and flat states, with the inter-point distance $\{A_1, C_0\}$ contracting from 53.7 mm (flat) to 45.2 mm (elevated). This contraction enables mechanical coupling to an elastic regulator at $\{A_1, C_0\}$ (Fig. S21A). During BOS pushing down, the regulator undergoes progressive stretching, storing elastic energy with a maximum strain of 0.19 (Fig. S21B). Pre-tensioning the regulator (Fig. S21A) introduces prestress into the system, amplifying stored elastic energy. The resulting prestrain accumulates linearly in the regulator's strain-position curve (Fig. S21C), demonstrating predictable energy storage behavior.

As the BOS elevates, elastic energy stored within the regulator releases to assist deployment, fundamentally reshaping the system's energy landscape. The energy curves in Fig. S21D are derived by integrating experimental force data from Fig. 3E. The negative values are from the directional convention conflict: the regulator applies upward force while the measurement protocol defines downward tension as positive. Consequently, greater energy release from the regulator yields more negative values. The curves at $\delta = 0$ mm maintain near-zero energy while producing significant decreases in the elevated state.

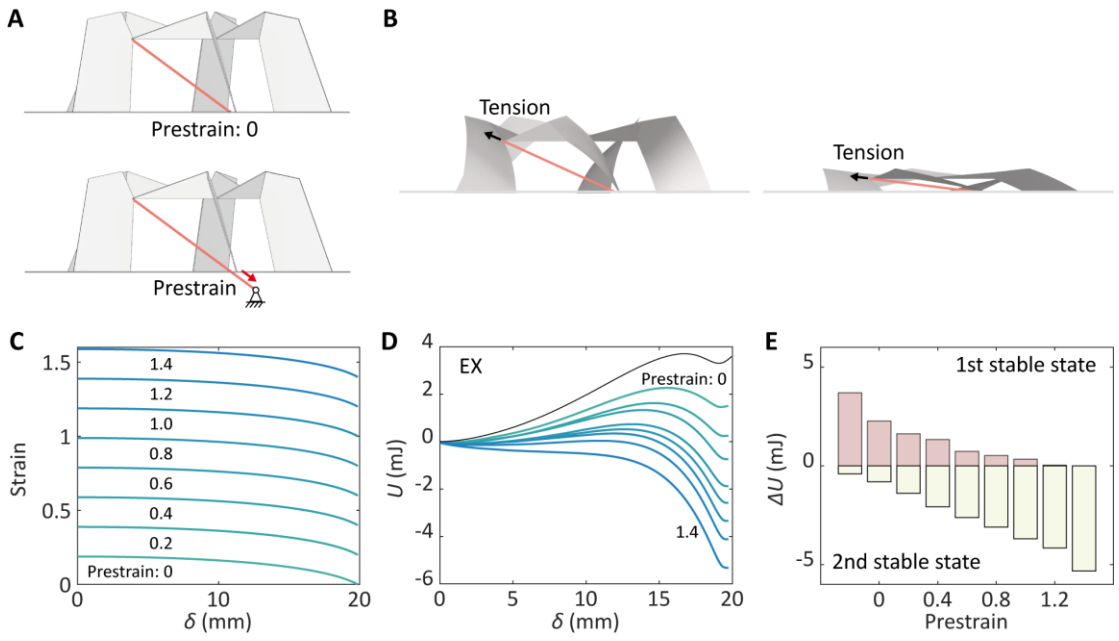


**Fig. S21.** Effect of embedding a regulator on the bistable origami metastructure. (A) Schematic of the initial state of the regulator. The regulator is installed at the two ends of an arm at the standing state. The regulator can be stretched to generate prestrain. (B)

Working principle of the regulator. The regulator is tensioning when the bistable origami metastructure pushed down. (C) Strain of the regulator versus the displacement of the bistable origami metastructure. (D) Total energy of the bistable origami metastructure with regulator. (E) Influence of the prestrain of regulator on the energy barrier of the structure.

Energy barrier transformations reveal critical prestrain effects. Without regulator, the BOS exhibits a high first energy barrier of 3.7 mJ that impedes elevation. Embedding a regulator and increasing prestrain reduces this initial barrier while elevating the second barrier. At prestrain of 1.2, the first barrier diminishes to 0.03 mJ (effectively eliminated) while the second barrier increases to 4.1 mJ. This barrier inversion demonstrates prestrain-enhanced bistable locking—where the structure becomes nearly self-deploying yet maintains bistability.

For a regulator undergoing simple uniaxial tensile deformation, the stored elastic energy is given by:

$$U_r = \frac{1}{2} k_r (\Delta l_r)^2 \tag{S55}$$

where $k_r$ is the stiffness of the regulator and is selected as 1.33 N/mm, $\Delta l_r = l_r - l_{r0}$ is the change in the distance between points $\{A_i, C_i\}$. The distance $l_r$ between points $\{A_i, C_i\}$ is defined as

$$l_r = \|A_1 C_0\| \tag{S56}$$

When the regulator is pre-tensioned by displacement $l_{pre}$, its tensile energy is expressed as:

$$U_r = \frac{1}{2} k_r (\Delta l_r)^2 + k_r l_{pre} \Delta l_r \tag{S57}$$

The total potential energy of BOS coupled to a pre-tensioned regulator becomes:

$$U_{total} = U + U_r \tag{S58}$$

The load-bearing capacity $M'$ and hinge resistance $T_{\gamma 3}$ at hinges $A_i A_{i+1}$ are analytically derived from the total energy gradient:

$$M' = -\min\left(\frac{dU_{total}}{d\delta}\right) \tag{S59}$$

$$T_{\gamma 3} = -\min\left(\frac{dU_{total}}{d\gamma_3}\right) \tag{S60}$$

where the negative sign arises from work-energy convention (resisting applied displacement).

The regulator significantly enhances the energy barrier of the second equilibrium state, enabling originally monostable BOS configurations to achieve bistable functionality, as demonstrated in Fig. S22. The upper monostable region remains unchanged due to inherent geometric constraints where excessive arm distortion still prevents elevating. The middle bistable region expands substantially into the lower monostable zone. As prestrain increases from 0 to 0.8, the bistable area grows by 14% to 41.2% of the design space, demonstrating the regulator's capacity to transform monostable structure into bistable systems.

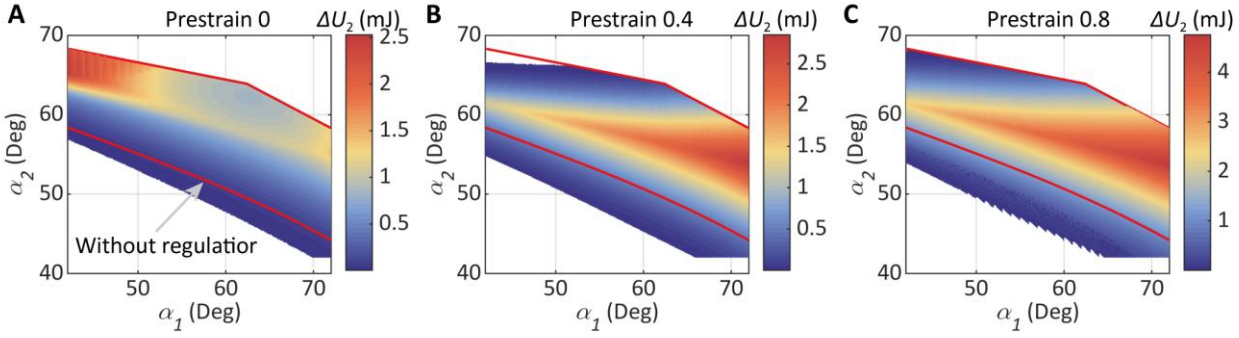


**Fig. S22.** Effect of regulator on the bistable range of geometric design.

Computational results in Fig. S23 demonstrate that both load-bearing capacity $M'$ and hinge resistance $T_{\gamma 3}$ scale linearly with regulator prestrain. Increasing prestrain elevates $M'$ from 0.4 N to 1.45 N while concurrently amplifying $T_{\gamma 3}$ from 1.3 N·mm to 4.8 N·mm, reflecting a 269% increase. This proportional enhancement confirms prestrain

actively modulates structural stiffness through energy gradient control.

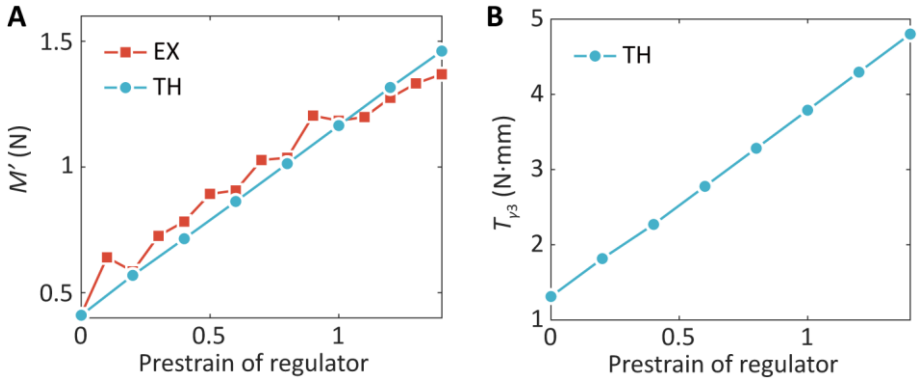


**Fig. S23.** Estimation of mechanical properties of the bistable origami metastructure with regulator. (A) Load bearing capability of the structure at the standing state. (B) Structural resistance of folding torque at the hinge $\gamma_3$.

**Supplementary Note 11: Additional explanation on thermal switch experiments**

The water-cooling head is offset upward by 8.5 mm from the base (Fig. S24) to allow a larger contact force, which shifts the ON position and reduces the contact gap to 8 mm. This optimized configuration aligns the ON position with the peak bistable force (Fig. S24). Under actuator pressure, a contact force of 0.5 N develops that simultaneously enhancing thermal performance and stabilizing the position.

The structural force curve serves as the critical boundary: BOS state transitions occur precisely when actuation forces intersect the boundary. By enveloping the structural force curve within the actuation force curves under high and low temperatures, where high-

temperature actuation forces exceed the structural peak while low-temperature forces remain below it, the peak of the structural force curve defines the switching threshold. This establishes stable switching temperatures at 25°C (OFF→ON) and 72°C (ON→OFF), creating a hysteretic control window resistant to thermal fluctuations.

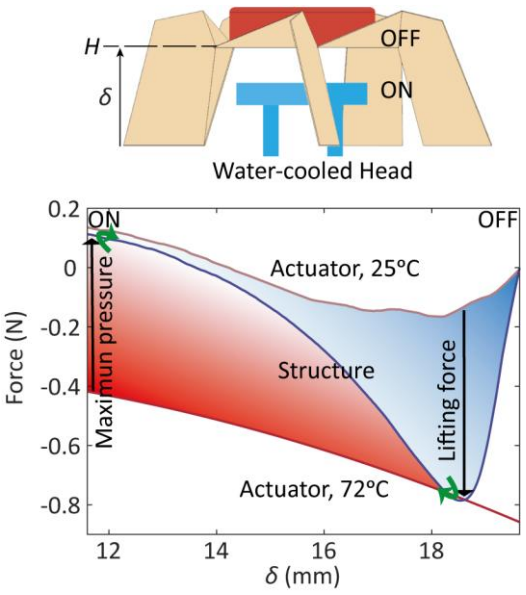


**Fig. S24.** Schematic of the demo design and the cycle mechanical switching.

The BOS switching speed is measured via side-view camera recordings (Fig. S25A) under varied heating powers (3W, 3.6W, and 8W). Higher power inputs accelerated heating rates, proportionally increasing switching speeds. Measured maximum device temperatures and corresponding average switching speeds are: 0.31 mm/s at 66°C, 0.66 mm/s at 73°C, and 1.16 mm/s at 115°C (Fig. S25B).

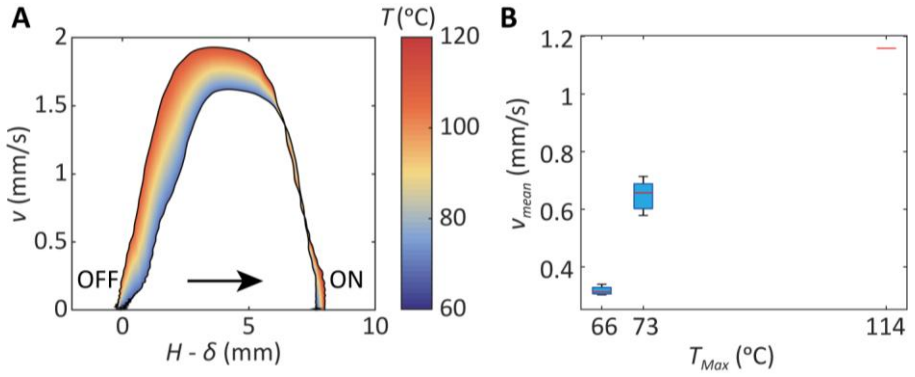


**Fig. S25.** Switching velocity of the bistable origami metastructure. (A) Displacement and temperature dependent velocity profile from OFF to ON states. (B) Average velocity at different rising temperature.

By precisely controlling the phase transition characteristics of the shape memory alloy (SMA), we demonstrate direct tunability of the BOS switching thresholds. When the SMA's phase transition temperature is reduced from 60°C to 47°C, the high-temperature switching threshold decreases from 73°C to 63°C, and the low-temperature threshold decreases from 25°C to 21°C (Fig. S26).

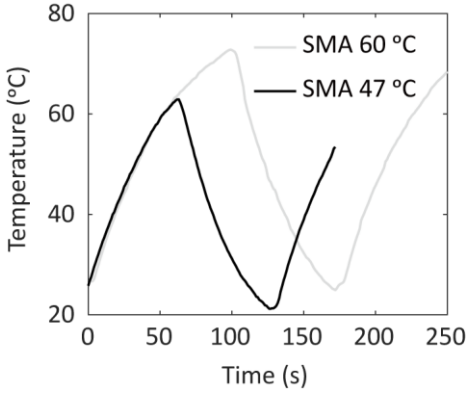


**Fig. S26.** Transient temperature curves of a heater on the BOS using SMA with different

phase transition temperature.

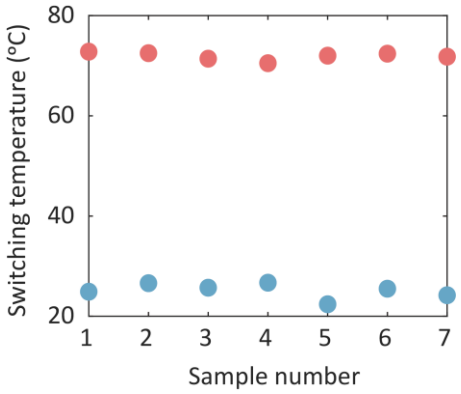


**Fig. S27.** Switching temperature of BOS under different fabrication batches.

**Table S2.** Comparative summary of response time, switching ratio, and actuation mechanisms of thermal switches reported under ambient and vacuum conditions (with intrinsic switching behavior not influenced by air treated as vacuum operation).

| **Thermal switch** | **Active or Passive** | **Vacuum or Air** | **Response time** | **Switch ratio** | **Mechanism** | **Sources** |
|---|---|---|---|---|---|---|
| SMA-1 | Active | Air | ~10s | 12 | Voltage-actuated, contact/non-contact | *Cell Reports Physical Science* 3, 100960 (2022). |
| Liquid metal droplet | Active | Air | ~5s | 71.3 | Hydraulic, electrostatic or gravity driven liquid metal droplet position change | *Appl. Phys. Lett.* 5, 112, 063505 (2018). |
| Compressible graphene composite foams | Active | Air | ~22min | ~8 | Compression-induced thermal conductivity change | *Nat Commun* 12, 4915 (2021). |
| Kevlar Nanofiber Aerogel | Active | Air | ~40s | 7.5 | Compression-induced thermal conductivity change | *Adv. Mater.* 35, 2207638 (2023). |
| SMA-2 | Passive | Air | 10-20s | ~40 | SMA/spring- | *Nature Energy* 3, |

| | | | | | | |
|---|---|---|---|---|---|---|
| | | | | | induced | 899–906 (2018). |
| PNIPAm hydrogel | Passive | Air | ~25min | 3.6 | Temperature-induced thermal conductivity change | *J. Phys. Chem. C* 123, 51, 31003–31010 (2019). |
| DTE-HS | Passive | Air | 12min | 390.3 | Passively actuated differential thermal expansion | *Appl. Therm. Eng.* 113, 1242 (2017). |
| Wax-motor | Passive | Air | / | 17.5 | Contact controlled | *ACS Eng. Au* 3, 2, 76–83 (2023). |
| Microsphere | Passive | Air | 30s | 16.26 | Thermal expansion-induced delamination | *Nat Energy* 9, 939–946 (2024). |
| Thermomagnetic actuation | Passive | Air | 2min | 2.1 | Thermomagnetic effect | *Cell Reports Physical Science* 4, 9, 101556 (2023). |
| ***This work*** | **Passive** | **Air** | **~10s** | **1360** | **SMA driven bistable origami metastructure** | / |
| $PbZrO_3$ | Active | Vacuum | ~150ns | 2.2 | E-field controlled AFE– | *Science* 382,1265-1269 |

| | | | | | | |
|---|---|---|---|---|---|---|
| | | | | | FE phase transition | (2023). |
| $MoS_2$ | Active | Vacuum | 15min | 10 | electrochemical controlled | *Nat. Commun.* 9, 4510 (2018). |
| $Ca_9La_5Cu_{24}O_{41}$ multilayer | Active | Vacuum | 30min | 2.3 | E-field controlled | *Sci. Rep.* 10, 14468 (2020). |
| SrCoOx | Active | Vacuum | 3min | 4 | electrochemical controlled | *Adv. Funct. Mater.* 33, 2214939 (2023). |
| ELST | Active | Vacuum | 10s | 14.2 | Strain/temperature-induced thermal conductivity change | *Nat Commun* 15, 5590 (2024). |
| Three-terminal magnetic thermal transistor | Active | Vacuum | ~17min | 109 | Magnetically actuated | *Nat Commun* 14, 393 (2023). |
| SMA-2 | Passive | Vacuum | 10-20s | 2070 | SMA/spring-induced | *Nature Energy* 3, 899–906 (2018). |
| Thermomagnetic actuation | Passive | Vacuum | 2min | 34 | Thermomagnetic effect | *Cell Reports Physical Science* 4, 9, 101556 (2023). |

| | | | | | | |
|---|---|---|---|---|---|---|
| ***This work*** | **Passive** | **Vacuum** | **~10s** | **13984** | **SMA driven bistable origami metastructure** | **/** |

**Reference**


1. L. S. Novelino, Q. J. Ze, S. Wu, G. H. Paulino, R. K. Zhao, Untethered control of functional origami microrobots with distributed actuation. *P Natl Acad Sci USA* **117**, 24096-24101 (2020).
2. Z. Raheem, *Standard Test Methods for Flexural Properties of Unreinforced and Reinforced Plastics and Electrical Insulating Materials 1* (2019).
3. A. Jain, K. E. Goodson, Measurement of the thermal conductivity and heat capacity of freestanding shape memory thin films using the 3ω method. *J Heat Trans-T Asme* **130**, 102402 (2008).
4. J. N. Sweet, E. P. Roth, M. Moss, Thermal-Conductivity of Inconel-718 and 304 Stainless-Steel. *Int J Thermophys* **8**, 593-606 (1987).
5. N. Chowdhury, J. C. Sun, D. G. Cahill, Anisotropic Thermal Conductivity of Kapton Films, Composites, and Laminates. *Acs Appl Polym Mater* **7**, 1440-1447 (2025).
6. T. Echániz, I. Setién-Fernández, R. B. Pérez-Sáez, M. J. Tello, Experimental verification of the anomalous skin effect in copper using emissivity measurements. *Appl Phys Lett* **102**, 244106 (2013).

7. K. Yu, H. Y. Zhang, Y. Liu, Y. F. Liu, Study of normal spectral emissivity of copper during thermal oxidation at different temperatures and heating times. *Int J Heat Mass Tran* **129**, 1066-1074 (2019).
8. M. L. Hao, J. Li, S. Park, S. Moura, C. Dames, Efficient thermal management of Li-ion batteries with a passive interfacial thermal regulator based on a shape memory alloy. *Nat Energy* **3**, 899-906 (2018).
9. Y. Chen, R. Peng, Z. You, Origami of thick panels. *Science* **349**, 396-400 (2015).
10. J. A. Faber, A. F. Arrieta, A. R. Studart, Bioinspired spring origami. *Science* **359**, 1386-1391 (2018).
11. K. Liu, T. Tachi, G. H. Paulino, Invariant and smooth limit of discrete geometry folded from bistable origami leading to multistable metasurfaces. *Nat Commun* **10**, 4238 (2019).
12. E. T. Filipov, K. Liu, T. Tachi, M. Schenk, G. H. Paulino, Bar and hinge models for scalable analysis of origami. *Int J Solids Struct* **124**, 26-45 (2017).
13. Z. R. Zhai, Y. Wang, H. Q. Jiang, Origami-inspired, on-demand deployable and collapsible mechanical metamaterials with tunable stiffness. *P Natl Acad Sci USA* **115**, 2032-2037 (2018).
14. K. Liu, F. Hacker, C. Daraio, Robotic surfaces with reversible, spatiotemporal control for shape morphing and object manipulation. *Sci Robot* **6**, eabf5116 (2021).